Article

Developmental Cell

Septins regulate border cell surface geometry, shape, and motility downstream of Rho in *Drosophila*

Graphical abstract

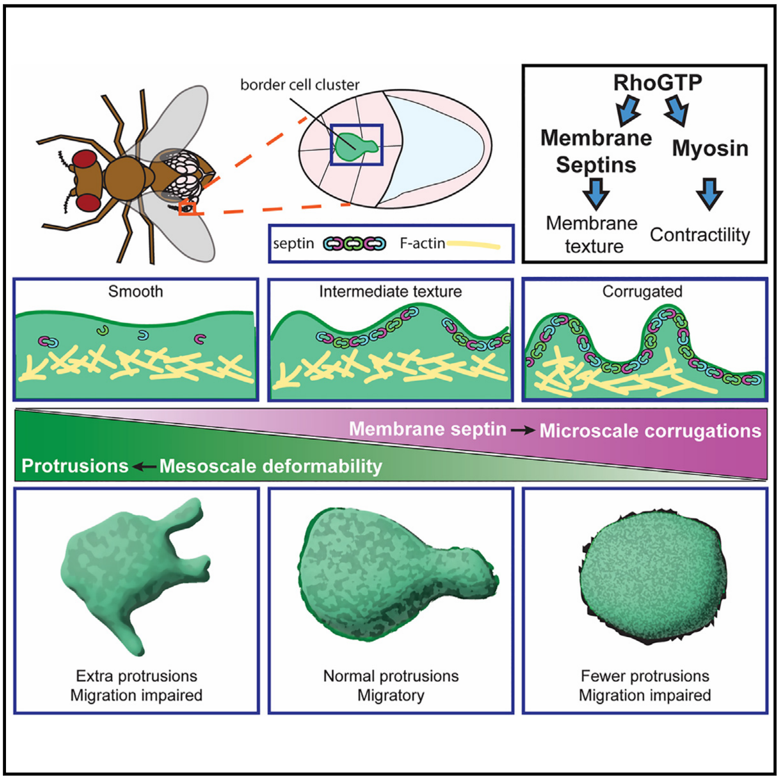

Highlights

- The *Drosophila* septins 1 and 2 and Pnut regulate border cell delamination and migration
- Active Rho independently recruits septins and myosin to border cell membranes
- GrabFP-mediated recruitment of septins to membranes rescues RhoN19 migration defects
- Membrane septins promote migration by regulating surface texture and deformability

Authors

Allison M. Gabbert,
Joseph P. Campanale,
James A. Mondo, ...,
Sebastian J. Streichan, Nina Miolane,
Denise J. Montell

Correspondence

dmontell@ucsb.edu

In brief

Using the *Drosophila* border cells as an *in vivo* model for confined, collective cell migration, Gabbert et al. show that septins are a major Rho effector. Active Rho recruits septins to the membrane where they regulate surface texture and deformability and thus cluster shape and motility.

Gabbert et al., 2023, Developmental Cell *58*, 1399–1413
August 7, 2023
https://doi.org/10.1016/j.devcel.2023.05.017

Developmental Cell

CellPress
OPEN ACCESS

Article

Septins regulate border cell surface geometry, shape, and motility downstream of Rho in *Drosophila*

Allison M. Gabbert,[1] Joseph P. Campanale,[1] James A. Mondo,[1] Noah P. Mitchell,[2,3] Adele Myers,[4]
Sebastian J. Streichan,[3] Nina Miolane,[4] and Denise J. Montell[1,5,*]
[1]Molecular, Cellular and Developmental Biology Department, University of California, Santa Barbara, Santa Barbara, CA 93106, USA
[2]Kavli Institute for Theoretical Physics, University of California, Santa Barbara, Santa Barbara, CA 93106, USA
[3]Physics Department, University of California, Santa Barbara, Santa Barbara, CA 93106, USA
[4]Electrical and Computer Engineering Department, University of California, Santa Barbara, Santa Barbara, CA 93106, USA
[5]Lead contact
*Correspondence: dmontell@ucsb.edu
https://doi.org/10.1016/j.devcel.2023.05.017

SUMMARY

Septins self-assemble into polymers that bind and deform membranes *in vitro* and regulate diverse cell behaviors *in vivo*. How their *in vitro* properties relate to their *in vivo* functions is under active investigation. Here, we uncover requirements for septins in detachment and motility of border cell clusters in the *Drosophila* ovary. Septins and myosin colocalize dynamically at the cluster periphery and share phenotypes but, surprisingly, do not impact each other. Instead, Rho independently regulates myosin activity and septin localization. Active Rho recruits septins to membranes, whereas inactive Rho sequesters septins in the cytoplasm. Mathematical analyses identify how manipulating septin expression levels alters cluster surface texture and shape. This study shows that the level of septin expression differentially regulates surface properties at different scales. This work suggests that downstream of Rho, septins tune surface deformability while myosin controls contractility, the combination of which governs cluster shape and movement.

INTRODUCTION

Cell migration is essential for development, wound healing, immune responses, and tumor metastasis (reviewed by SenGupta et al.,[1] Stuelten et al.,[2] Perez-Vale and Peifer,[3] Yamada and Sixt,[4] and Ridley et al.[5]). While our fundamental understanding of the molecular mechanisms controlling cell motility derives primarily from studying cells migrating individually on glass, *in vivo*, cells frequently move collectively (reviewed by Shellard and Mayor,[6] Haeger et al.,[7] Scarpa and Mayor,[8] and Mishra et al.[9]). *In vivo*, cells also move through complex, cell-rich microenvironments that are difficult if not impossible to recapitulate *in vitro*. Therefore, *in vivo* models amenable to genetic analysis and live imaging are important.

Border cells in the *Drosophila* egg chamber provide an excellent model to study collective cell migration.[10–14] The border cell cluster is composed of four to six migratory cells that surround and transport two non-motile polar cells from the anterior end of the egg chamber, in between nurse cells, to the oocyte during oogenesis (reviewed by Montell et al.[12]). Cytoskeletal dynamics are critical determinants of cell shape and movement in general[15,16] and border cells in particular,[17–23] where the *in vivo* requirement for the small GTPase Rac in F-actin-rich protrusions and migration was first demonstrated.[24]

F-actin, microtubules, and intermediate filaments are well-studied, dynamic polymers that contribute to cell shape and motility.[15] Septins are filament-forming GTPases that have been described as a fourth major cytoskeletal element.[25] First discovered as a key component required for septation in budding yeast,[26] septins are now known to be conserved throughout animals and fungi where they commonly localize to the cell cortex and act as protein scaffolds.[27] Septins regulate cell polarity, ciliogenesis, cytokinesis, individual and collective cell migrations, and other processes.[28–32] In addition to their functions in normal cellular processes, alterations in septin expression have been implicated in diseases including neurodegenerative diseases such as Alzheimer's and Parkinson's, many types of cancer such as mixed lineage leukemia and ovarian cancer, and in male infertility,[33–36] though the precise contributions of septins to disease etiology are not yet clear. Key open questions in the septin field include how the *in vitro* properties of septins relate to their *in vivo* functions, how alterations in septin expression levels affect their functions, and how septin activity is regulated *in vivo*.

Fruit flies have a simplified set of five septins compared with 13 encoded in the human genome. *Drosophila* Sep1, Sep2, and Pnut have been purified as a complex.[37] In an RNA expression screen, we previously reported that mRNAs encoding Sep1, Sep2, and

Developmental Cell 58, 1399–1413, August 7, 2023 © 2023 The Authors. Published by Elsevier Inc.

Pnut are expressed and/or enriched in border cells, whereas Sep4 and Sep5 were not detected.[38] Here, we show that Sep1, Sep2, and Pnut proteins are expressed in both cytoplasmic and membrane associated pools and that the active form of the GTPase Rho recruits septins to border cell membranes whereas dominant-negative Rho sequesters septins in the cytoplasm. We report that septins are required for border cell migration and that their knockdown makes outer border cell surfaces smoother, whereas their overexpression roughens them. Knockdown and overexpression also change the overall cluster shape and impair motility. Together these results demonstrate that septin levels tune cell surface topography and that precisely appropriate levels promote collective motility downstream of Rho.

RESULTS

Septins are present in cytoplasmic and membrane pools in collectively migrating border cells

Individual septin monomers contain a proline-rich amino-terminal region, a central core that includes a GTP-binding domain, and a carboxy-terminal region (Figure 1A). Septins oligomerize via interactions between the GTP-binding domains (G-G) and through the interactions between N and C termini of different subunits (N-C) (Figure 1B). Septin polymers can form filaments and more complex structures such as gauzes, bundles, and rings (Figure 1C).[39] *Drosophila* and human septins show between 55% and 73% amino acid sequence identity (Figure S1A).

Drosophila egg chambers are composed of ~850 somatic follicle cells that surround 16 germline cells—15 polyploid nurse cells and one oocyte (Figures 1D–1F). Border cells develop at the anterior end of the egg chamber and during stage 9 extend protrusions between the nurse cells (Figure 1D), delaminate from the epithelium, and migrate down the central path (Figure 1E) until they reach the oocyte at stage 10 (Figure 1F). To probe the expression and localization of septins in egg chambers, we examined a transgenic insertion of Sep2, expressed under its own regulatory sequences, and tagged with GFP. Sep2::GFP is expressed in all follicle cells (Figures 1D–1F), including border cells, throughout their migration (Figures 1D′–1F′).

Septins are present in both cytoplasmic and membrane pools (Figures 1G and 1G′). Septins are more enriched at membranes, co-localizing with the plasma membrane marker phospholipase C delta PHGFP (PLCδGFP), at contacts between border cells and nurse cells (Figure 1H) than at membranes where border cells contact other border cells (Figure 1I).

Septins are required for border cell migration

To test whether septins play a role in border cell migration, we knocked down Sep1, Sep2, or Pnut using UAS-RNAi constructs. RNAi hairpins were expressed in combination with a UAS-LifeActGFP marker using c306Gal4. In egg chambers expressing the control (white) RNAi, the border cell cluster completes migration to the oocyte by stage 10 (Figure 2A). Expressing RNAi against Sep1, Sep2, or Pnut impaired migration (Figures 2B–2D). Interestingly, overexpression of Sep1 or Sep2 using c306Gal4 also disrupted migration (Figures 2E and 2F). We quantified the phenotypes using categories that denote how far the cluster migrated by stage 10 (Figures 2G and 2H). Thus, Septins 1 and 2 and Pnut are required for border cell migration, and the level of septin expression must be regulated, with too much or too little septin impeding motility.

Border cell migration is a multistep process that begins with their specification and rounding up, followed by a delamination phase, in which the cluster invades between nurse cells and detaches from the anterior epithelium (Figure 2I; Video S1). Upon Sep1, 2, or Pnut knockdown, the border cell cluster still rounded up and the cells upregulated expression of the marker Singed, which is the fly homolog of the actin-binding protein Fascin (Figures S2A–S2D). However, septin knockdown impaired delamination (Figure 2J; Video S2). Septin overexpression also caused delamination defects (Figure S2E; Video S3). Delamination is normally followed by migration, in which the cluster actively squeezes in between the nurse cells toward the oocyte (Figure 2K; Video S4).[40] Of those septin knockdown or overexpression clusters that detached, many (30%–70%) failed to migrate normally (Figures 2L and S2F; Videos S5 and S6). Therefore, optimal septin expression is required for detachment and migration.

Septins 1, 2, and Pnut are interdependent

Septins assemble into heteromeric complexes in many contexts,[27,41] and loss of a single septin can lead to destabilization of the complex.[42–44] To compare the Sep2::GFP and Pnut expression patterns, we stained egg chambers expressing Sep2::GFP for Pnut and used Airyscan confocal imaging (Figures S3A–S3A″). Sep2 and Pnut significantly colocalized (Figures S3A–S3C), consistent with previous reports of Sep2 assembly with Sep1 and Pnut into filaments.[37,45,46]

To test whether the septin protein abundances depend on one another in follicle cells, we expressed Sep1, Sep2, or Pnut RNAi in clones within the follicular epithelium and stained with an antibody against Pnut. Sep1 or Sep2 RNAi reduced Pnut protein levels compared with neighboring control cells (Figures 3A–3D′ and 3I). We observed similar results within the border cell cluster (Figures 3E–3H′ and 3J). Quantification of the results showed that while Pnut knockdown reduced Pnut expression the most, knockdown of either Sep1 or Sep2 significantly reduced Pnut expression (Figures 3I and 3J). Similarly, border cells homozygous mutant for Sep2 exhibited reduced levels of Pnut in clonal cells (Figures S3D–S3E′). These results establish the effectiveness of the RNAi knockdowns and suggest that Sep1, Sep2, and Pnut are interdependent.

Similarly, c306Gal4-driven RNAi against Sep1 or Sep2 in the posterior follicle cells significantly decreased Pnut expression (Figures 3K and S3F–S3I). Additionally, knockdown of Sep1 and Pnut using c306Gal4 in a Sep2::GFP background significantly decreased GFP expression in the posterior follicle cells (Figures 3L and S3J–S3M). Therefore, we conclude that Sep1, Sep2, and Pnut depend on each other, are likely to function in a complex, and are more stable when assembled.

Septins and myosin colocalize dynamically

At the yeast bud neck, active Cdc42 recruits septins,[47] which in turn recruit myosin.[48] To investigate the regulation of septins in border cells, we generated clones of cells expressing constitutively active or dominant negative forms of Cdc42 or one of two different Cdc42RNAi constructs in the follicular epithelium of the egg chamber (Figures S4A–S4D′) and the border cells

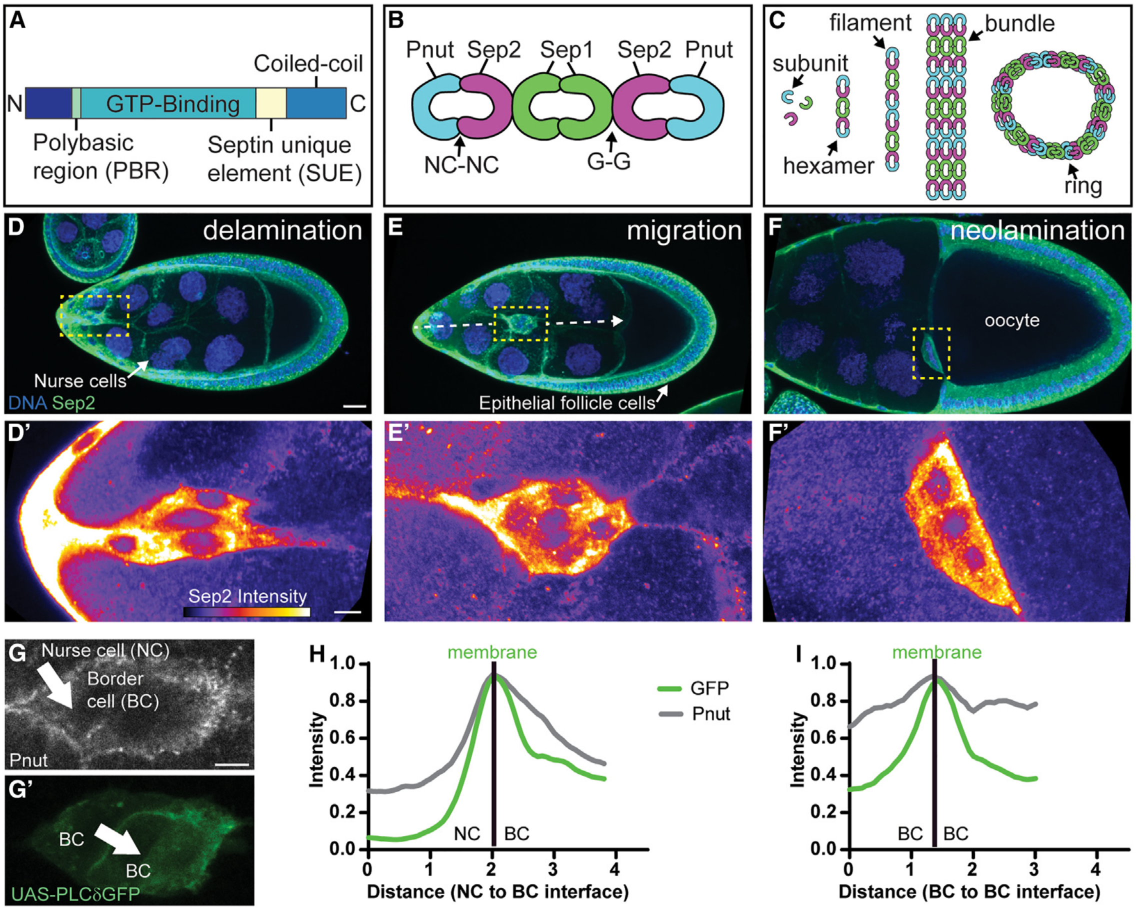

Figure 1. Septins localize in cytoplasmic and membrane pools throughout border cell migration

(A) Schematic of septin protein domains.

(B) Septins assemble into complexes through interactions between their N-C and G-G interfaces. In *Drosophila*, Pnut, Sep2, and Sep1 form a complex.

(C) Septin filaments can form higher order structures.

(D–F) Maximum intensity projections of egg chambers labeled with Hoechst (blue) and Sep2::GFP (green). (D′–F′) Single slices of the border cell clusters from (D)–(F) with Sep2:GFP shown in fire LUT (pseudocolor image fire Look-Up Table). The direction of migration is left to right.

(G) (G and G′) Single slice of a migrating border cell cluster labeled with Pnut (G) and UAS-PLCδGFP, a membrane marker (G′).

(H and I) Graph of representative line scans of Pnut and PLCδGFP intensities across the nurse cell to border cell interface (H) or border cell to border cell interface (I). Scale bars: 20 μm in (D) and 5 μm in (D′) and (G).

(Figures S4F–S4I′). We did not detect any measurable change in Pnut expression or localization in clones, compared with neighboring control cells (Figures S4E and S4J). While we cannot rule out a contribution from Cdc42, the effect—if any—is too subtle to account for the observed border cell migration defects. In addition, Cdc42 knockdown affects cluster cohesion, which is distinct from the septin loss-of-function phenotype in the border cells. Therefore, Cdc42 and septins appear to function separately in border cells.

Myosin II was another candidate for interacting with septins, as septins scaffold myosin in yeast and mammalian cells.[48,49] Septin 7 is essential for planar polarization of active myosin during convergent extension movements in *Xenopus* gastrulation,[31] and myosin regulates border cell detachment and protrusion dynamics.[50] To observe myosin expression and localization, we used flies expressing a tagged third copy of spaghetti squash (Sqh), which encodes the regulatory light chain of non-muscle myosin II. Myosin is highly dynamic in the migrating border cell cluster, appearing as moving "myosin flashes,"[22,51] so we conducted live imaging of clusters expressing both Sqh::mCherry (Figure 4A) and Sep2::GFP (Figure 4A′). We imaged at 15-s intervals to capture the rapid myosin flashes along the periphery. Sep2 and Sqh traveled together dynamically (Figure 4B). This dynamic colocalization suggested a possible link between septins and myosin.

Different mechanisms might account for septin and myosin colocalization (Figure 4C). By analogy to the bud neck in budding yeast,[48,52] septin might recruit myosin. Alternatively, myosin might recruit septin. A third option is that both septins and myosin might both be recruited by an unknown upstream regulator (Figure 4C), or myosin and septin might have colocalized by chance.

To test whether myosin regulates septin expression or localization, we generated clones of cells expressing RNAi against Sqh in the follicular epithelium (Figures 4D–4F′) and in border

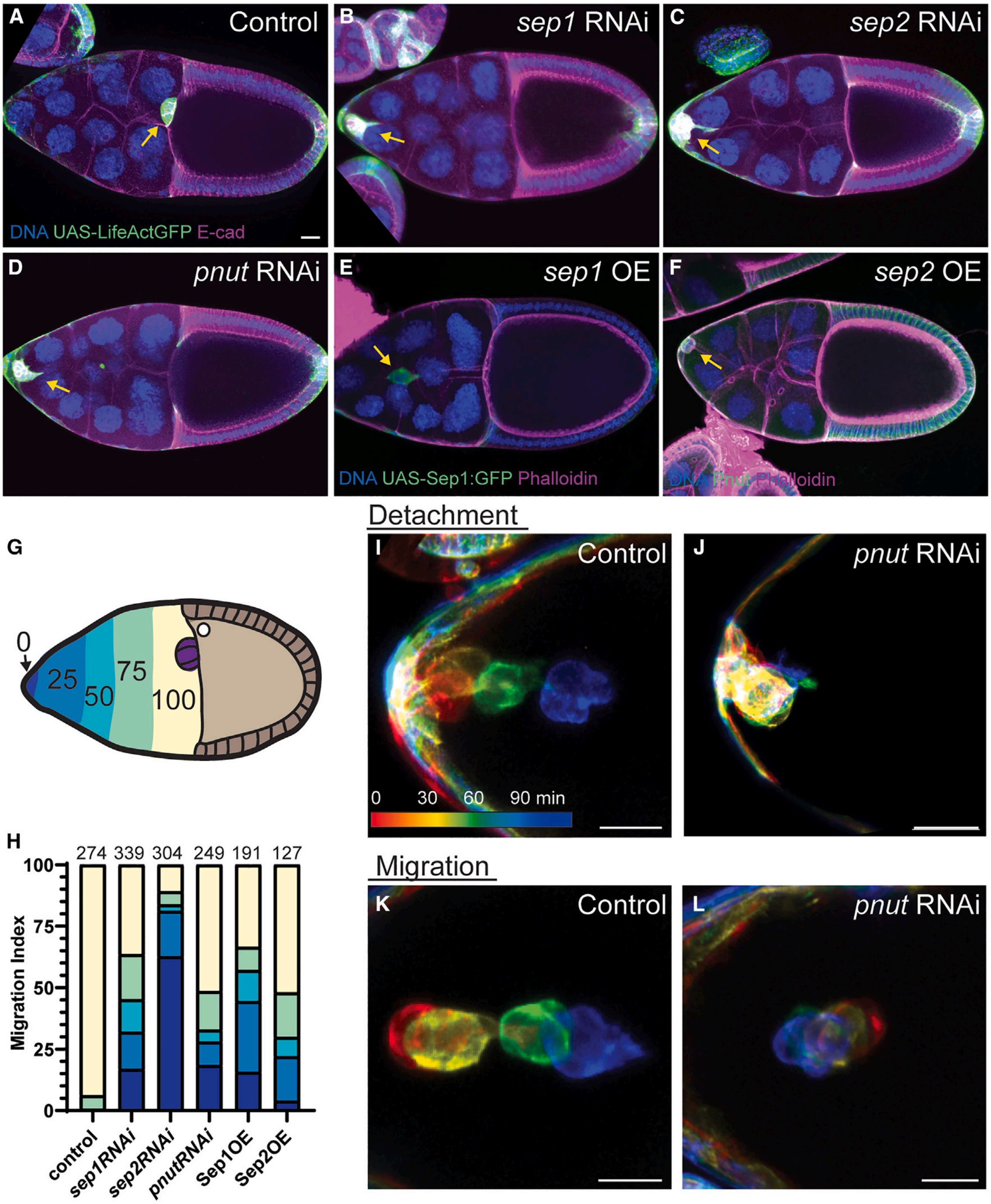

Figure 2. Septins are required for border cell migration

(A–D) Maximum intensity projections of stage 10 egg chambers expressing UAS-LifeActGFP and UAS-whiteRNAi (A, control) or septinRNAi (B–D) in the border cell cluster by c306Gal4. Hoechst (blue) and E-cadherin (magenta).

(E and F) Projections of stage 10 egg chambers expressing (E) UAS-Sep1::GFP (overexpression) and (F) UAS-Sep2 (overexpression) by c306Gal4. Hoechst (blue) and Phalloidin (magenta). Arrows (A–F) denote border cell clusters.

(G) Schematic of a stage 10 egg chamber. Colors indicate the percentage of migration path.

(H) Quantification of border cell migration in egg chambers after RNAi knockdown or overexpression of the indicated septins. The control was whiteRNAi.

(I–L) Temporally color coded projections from movies of border cell detachment (I and J) or migration (K and L). Control (whiteRNAi) or septin knockdown clusters. Scale bars: 20 μm in (A) and (I)–(L). The migration direction is left to right.

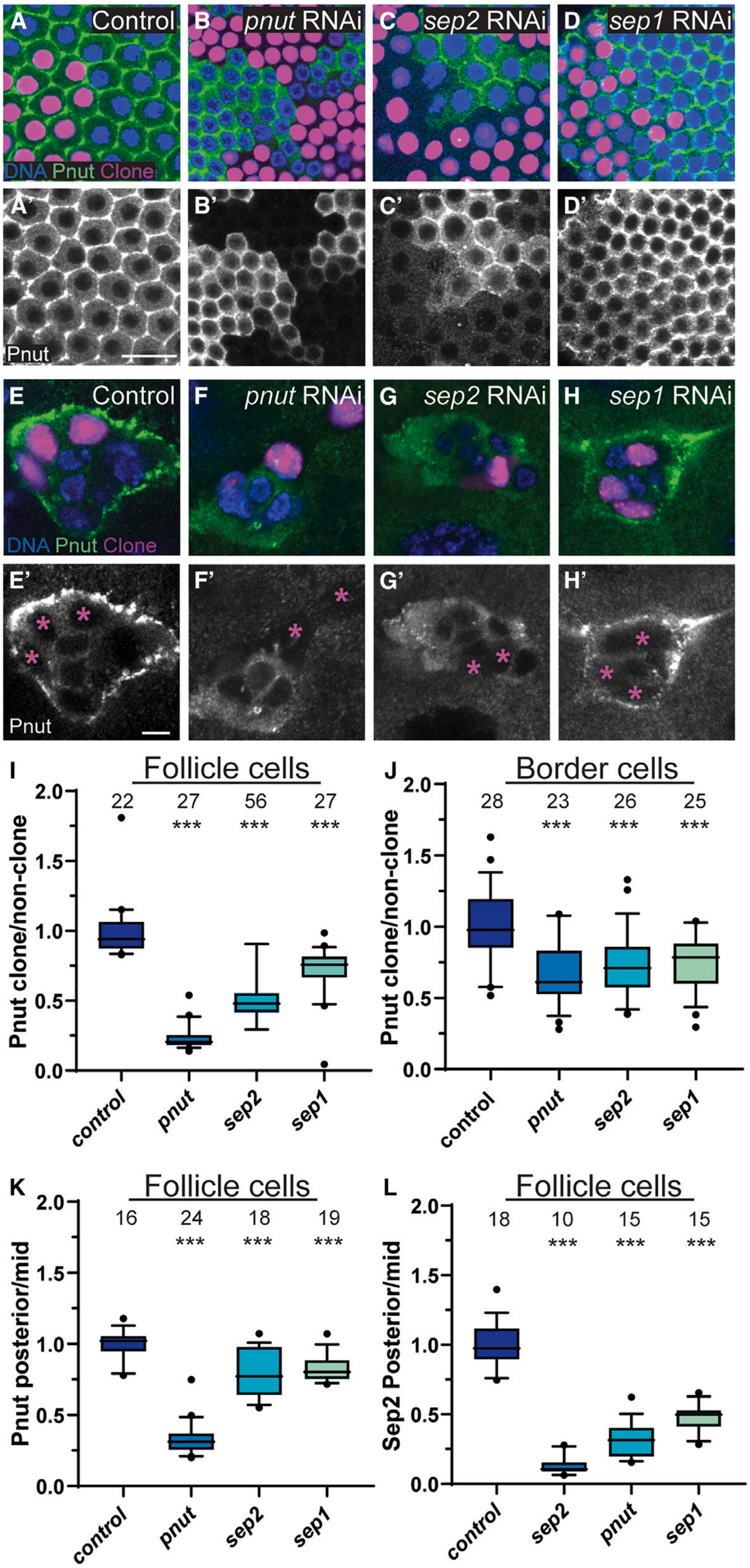

Figure 3. Septins 1, 2, and Pnut are interdependent

(A–H) (A–D) Images of basal surface of epithelial follicle cells or (E–H) border cells clonally expressing UAS-whiteRNAi (control) or septinRNAi labeled with Hoechst (blue) and Pnut (green). Clones expressing RNAi and UAS-nuclear-localized RedStinger (magenta). (A′–D′) and (E′–H′) Pnut staining (gray) from (A)–(D) and (E)–(H), respectively. Border cell clones are marked with magenta asterisks.

(I–K) Boxplots of Pnut intensity in clones compared with non-clones for (I) follicle cells, (J) border cells, and (K) posterior follicle cells.

(L) Quantification of Sep2:GFP intensity in posterior follicle cells expressing RNAi compared with follicle cells not expressing RNAi.

(I–L) Three asterisks represent $p < 0.001$ when analyzed by an ordinary one-way ANOVA, followed by Tukey post-hoc analysis. Scale bars: 20 μm in (A′) and 5 μm in (E′). The whiskers represent the data from the 10-90th percentile

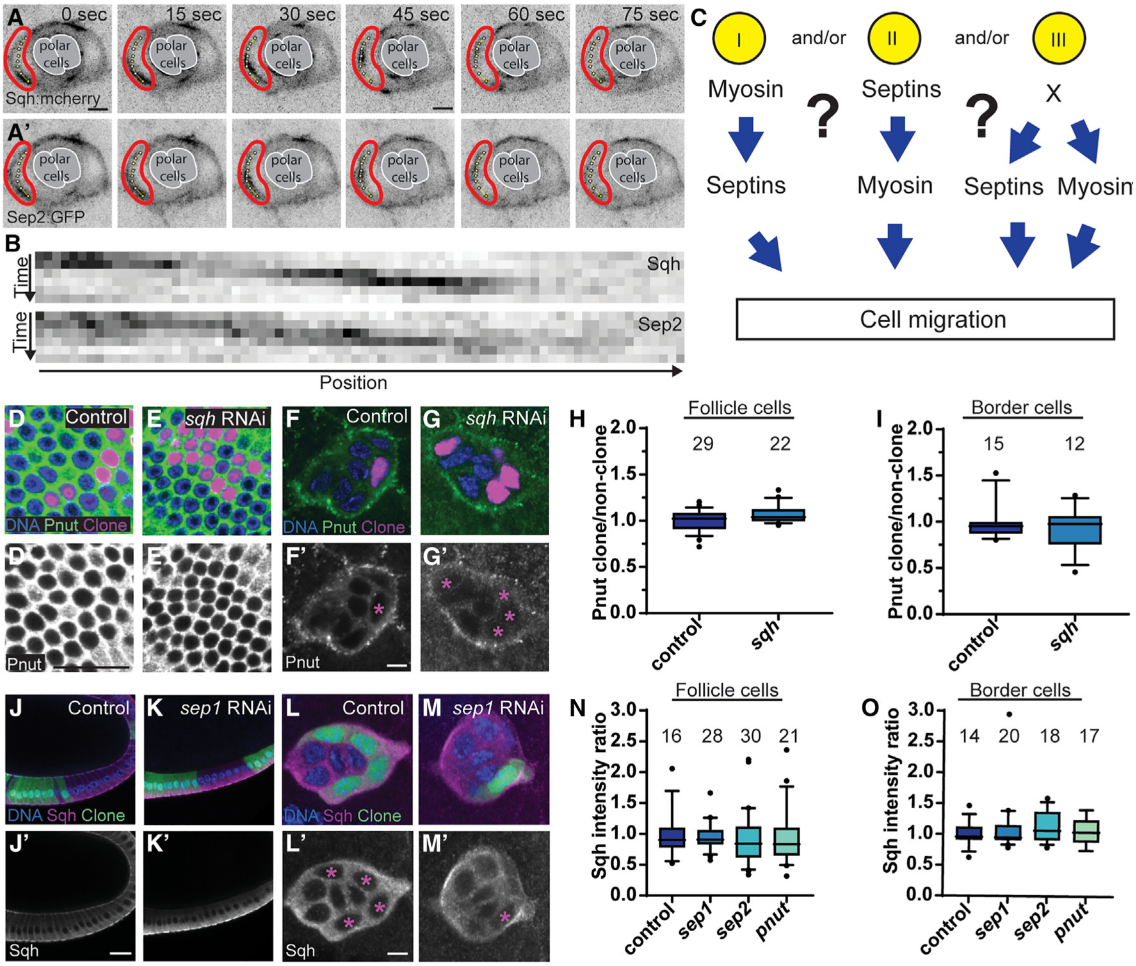

Figure 4. Septins and myosin colocalize dynamically independent of one another

(A) (A and A′) Maximum intensity still images from time lapse movies of migrating border cells labeled with Sqh:mCherry (A) and Sep2::GFP (A′). The central polar cells are masked.

(B) Kymographs of Sqh and Sep2, where the measured area is denoted by a dotted line, outlined in red in (A) and (A′).

(C) Three possible models to describe the relationship between septins and myosin in border cells.

(D and E) Single z slice confocal images of epithelial follicle cells on the basal surface of the egg chamber clonally expressing UAS-sqhRNAi labeled with Hoechst (blue) and Pnut (green). Clones are marked with magenta nuclei, expressing nuclear-localized UAS-RedStinger. (D′ and E′) Images from (D) and (E) for Pnut (gray).

(F and G) Same as (D) and (E) but in border cells. (F′ and G′) Same images from (F) and (G) but only labeled with Pnut (gray). Clones are marked with magenta asterisks.

(H and I) Boxplots of Pnut intensity in clones compared with non-clones in follicle cells (H) and border cells (I). The whiskers represent the data from the 10-90th percentile

(J and K) Single slices of epithelial follicle cells clonally expressing UAS-septin RNAi and UAS-GFP labeled with Hoechst (blue). All cells express sqh:mcherry. (J′ and K′) Same images from (J) and (K) but only labeled with Sqh (gray).

(L and M) Same as (Q) and (R) but in border cells. (L′ and M′) Same images from (Q) and (R) labeled with Sqh (gray). Clones are marked with magenta asterisks.

(N and O) Boxplots of Sqh intensity in clones compared with non-clones in follicle cells (N) and border cells (O). Scale bars: 5 µm in (A), (F′), and (L′) and 20 µm in (D′) and (J′). The whiskers represent the data from the 10-90th percentile

cells (Figures 4F–4G′). We did not detect any change in Pnut expression level or localization in the basal follicular epithelium (Figure 4H) or in border cells (Figure 4I). To test whether septin regulates myosin, we clonally knocked down septin in the follicle cells (Figures 4J–4K′) and border cells (Figures 4L–4M′) in a Sqh::mCherry background and detected no difference in fluorescence intensity (Figures 4N and 4O). Furthermore, we could detect no time delay between the appearance of septin and myosin flashes.

Myosin and E-cadherin (E-cad) colocalize at border cell to border cell interfaces,[22] so we tested for a relationship between E-cad and septins. Colocalization analysis of E-cad and the membrane marker PLCδGFP in control (Figures S4K and S4K′), septin knockdown (Figures S4L and S4L′), and septin overexpression (Figures S4M and S4M′) border cell clusters showed no significant change in E-cad localization with altered septin expression (Figure S4N). 100% of E-cad RNAi-expressing clusters fail to complete migration. Neither Sep2 overexpression nor

Sep2RNAi modified the phenotype (Figure S4O). We conclude that Septin and E-cad function independently in border cells.

Active Rho recruits septins to membranes

We considered that septins and myosin might be recruited to the cluster surface simultaneously by a common upstream regulator. The GTPase Rho stood out as a potential candidate, as it is a well-established regulator of myosin activity.[16] Rho has also been linked to septins in a few studies: for example, in rat embryonic fibroblast cells,[53] animal cell cytokinesis,[54] and in fission yeast at high temperature.[55] To test the effect of Rho activity on septin localization, we expressed dominant-negative Rho^{N19} (RhoDN) or constitutively active Rho^{V14} (RhoCA) in the border cell cluster and stained for Pnut. Pnut is typically present diffusely throughout the cytoplasm as well as in cytoplasmic puncta and is enriched at border cell to nurse cell interfaces but not border cell to border cell contacts (Figures 1G–1I and 5A). In Rho^{N19}-expressing border cell clusters, we observed a marked decrease in Pnut at nurse cell to border cell contacts (Figure 5B), whereas in Rho^{V14}-expressing clusters, we saw increased cortical Pnut (Figure 5C).

To quantify the effects of Rho activity on septin localization, we generated line scans of Pnut and the membrane marker PLCδGFP across nurse cell to border cell interfaces and adjacent cytoplasm as well as border cell to border cell interfaces and adjacent cytoplasm. We measured control, RhoCA, and RhoDN-expressing clusters (Figures S5A–S5F′). Using PLCδGFP as a proxy for membranes, we calculated the membrane to cytoplasmic ratio of Pnut intensity for each genotype. Quantification of the membrane to cytoplasmic ratio (Figures 5D and 5E) showed that the Rho^{N19}-mediated decrease in membrane associated Pnut was most evident at nurse cell to border cell contacts where Pnut is normally enriched (Figures 5A, 5B, and 5D). In contrast, the Rho^{V14}-mediated increase was particularly obvious at border cell to border cell contacts where Pnut is normally low (Figures 5A, 5E, and S5D–S5F′) and where two labeled membranes were juxtaposed (Figures 5C and 5E). Conversely, the abundance of cytoplasmic septin puncta was significantly higher when in the presence of Rho^{N19} and lower in the presence of Rho^{V14} (Figure 5F). Sep2::GFP colocalized with Pnut in all genotypes (Figure 5G), indicating that septins are mostly detected in multimeric assemblies. We conclude that Rho activity recruits septins to border cell membranes.

Rho kinase (Rok) functions downstream of Rho to phosphorylate myosin light chain kinase and thereby activate Sqh and myosin contractility. To test whether septin membrane localization responds to Rok activity, we generated clones of cells expressing constitutively activated Rok (RokCA), dominant-negative Rok (RokDN), or Rok RNAi and compared septin levels and localization. Control clones expressing GFP and an RNAi targeting the white gene exhibited septin levels and localization indistinguishable from neighboring non-expressing cells (Figures S4P and S4P′). Similarly, neither RokCA, nor RokDN, nor RokRNAi detectably altered septin expression or localization. We conclude that Rho recruits septins to the plasma membrane independently of Rok.

To test the functional consequences of septin membrane localization for border cells, we took advantage of the GrabFP system, which enables recruitment of GFP-labeled proteins to specific subcellular locations.[56] We previously established the effectiveness of GrabFP in border cells.[57,58] As illustrated in Figure S5G, we used a membrane tethered anti-GFP single chain nanobody in combination with Sep2::GFP to relocalize the diffusely cytoplasmic pool of Sep2::GFP (Figure S5H) to the membrane (Figure S5I). Since Sep1, Sep2, and Pnut assemble into a complex and stabilize one another, we expected that membrane-tethering one subunit would nucleate assembly sites and/or tether existing filaments. As expected, Pnut substantially colocalized with Sep2::GFP (Figures S5H–S5I″). Remarkably, septin membrane tethering significantly improved the migration of RhoN19-expressing border cells from <50% to >80% complete migration at stage 10 (Figure 5H), compared with an irrelevant GFP-tagged protein Cdep. By contrast, Sqh::GFP did not rescue. We conclude that septin is a major downstream effector of Rho for border cell migration and that the most biologically significant effect of Rho on septin is membrane recruitment.

To further explore the relationship between myosin and septin, we tested the effect of Sep2::GFP overexpression in clusters expressing a phosphomimetic and thus hyperactivated Sqh (SqhEE). SqhEE expression alone causes a significant migration defect, which Sep2 overexpression exacerbated (Figure 5I).

Moesin links cortical F-actin to the plasma membrane, and moesin RNAi impedes border cell migration. We found that septin overexpression significantly, albeit partially ameliorates the migration defect (Figure 5J) and alters the morphology of the ectopic protrusions (Figures S5J and S5K). In contrast, septin RNAi did not ameliorate the very strong migration defect caused by hyperactivated moesin (MoeCA) (Figure 5J). Septin RNAi did however modify the morphology of clusters expressing MoeCA, which typically exhibit abnormally long and thin protrusions that were rare when Sep2 was knocked down (Figures S5L–S5N). These results are consistent with the idea that septins and moesin serve related but not identical functions in regulating the cortex.

Septin knockdown and overexpression alter cluster shape

Border cell clusters change shape dynamically as they move. To initiate migration, one or two cells extend and retract forward-directed protrusions.[24,40,59] When a single leader is established, it communicates direction to the rest of the cells,[60] inhibiting them from forming leader-like protrusions.[19,61,62] Followers instead engage in crawling behaviors that both promote cluster cohesion and movement.[58] Leader protrusions act as sensory structures, probing the environment for chemical and physical cues.[22,63] In contrast to wild-type controls (Figure 6A), clusters with reduced septin expression adopted abnormal shapes, particularly ectopic protrusions (Figure 6B), similar to the phenotype previously described for inhibition of myosin heavy or light chain.[22] Conversely, overexpression of septin resulted in a rounder morphology (Figure 6C).

To gain deeper insight into the normal functions of septins in controlling cluster shape, we compared cluster geometries as well as the shape variation within and between control, knockdown, and overexpression groups. We first converted maximum intensity projections of border cell clusters (Figures 6A–6C) to binary masks to define the cluster boundaries (Figures 6A′–6C′ and

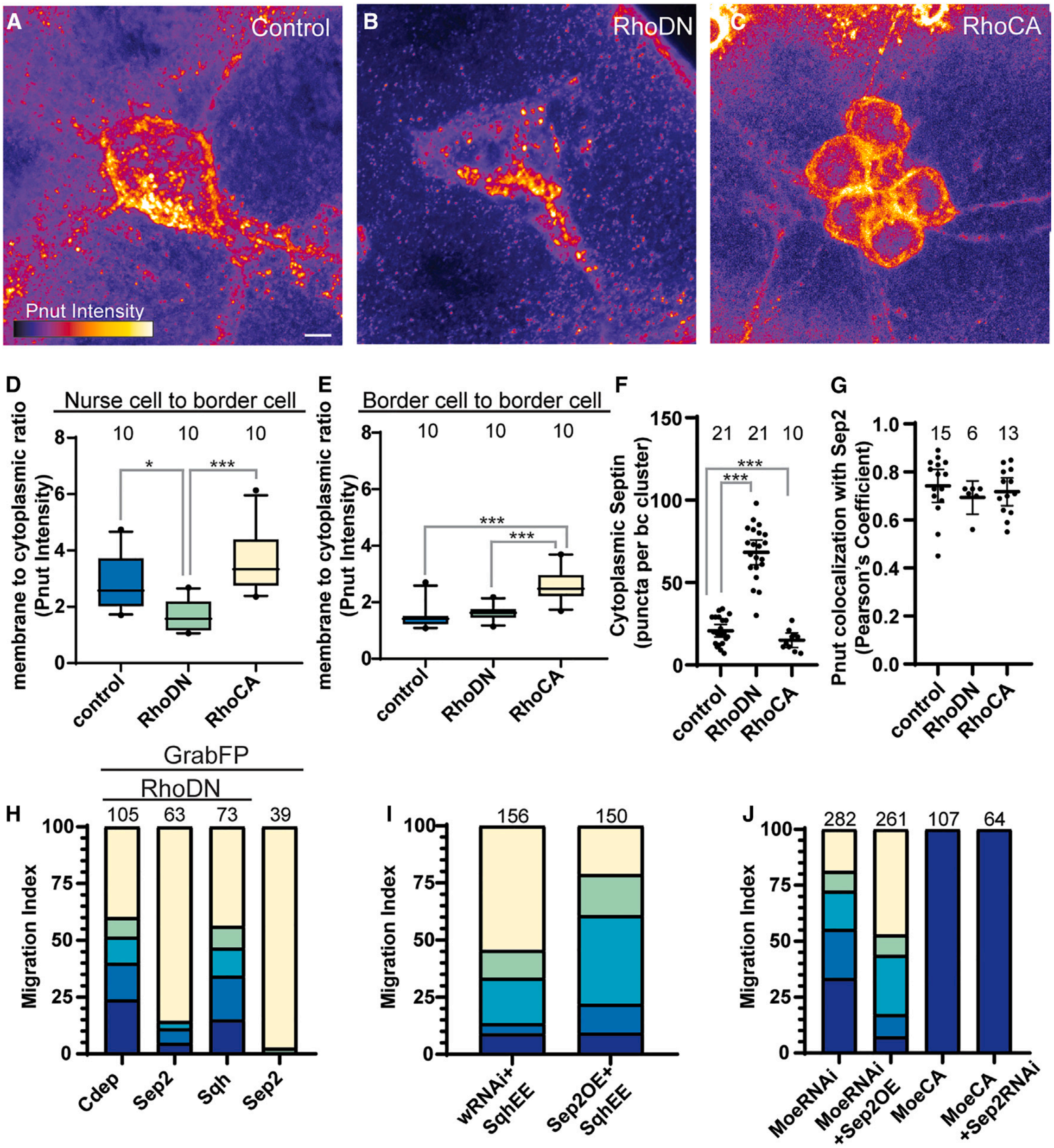

Figure 5. Rho regulates septins and myosin independently

(A–C) Maximum intensity projections of (A) control border cell cluster or clusters expressing (B) dominant negative Rho (UAS-RhoDN, i.e., RhoN19) or (C) constitutively active Rho (UAS-RhoCA, i.e., RhoV14) with Pnut protein expression shown by a fire LUT.

(D and E) Boxplots of membrane to cytoplasmic ratio of Pnut intensity across (D) nurse cell to border cell interfaces or (E) border cell to border cell interfaces. *$p < 0.05$ and ***$p < 0.001$ when analyzed by an ordinary one-way ANOVA, followed by Tukey post-hoc analysis. Error bars are 95% confidence intervals. The whiskers represent the data from the 10-90th percentile

(F) Counts of septin puncta in the cytoplasm of the border cell cluster. Each dot represents a cluster. ***$p < 0.001$ when analyzed by an ordinary one-way ANOVA, followed by Games-Howell's post-hoc analysis. The lines represent the mean with 95% confidence interval.

(G) Pearson's coefficient showing the colocalization of Pnut and Sep2. Each dot represents a cluster. The lines represent the mean with 95% confidence interval.

(H) Quantification of border cell migration in egg chambers expressing Cdep:GFP, Sep2:GFP, or Sqh:GFP with border cell clusters expressing UAS-RhoDN and/or the GrabFPIntra construct.

(I) Quantification of border cell migration in egg chambers with border cell clusters expressing UAS-SqhE20E21, a phosphomimetic version of Sqh, along with either UAS-white RNAi as a control for the number of UAS transgenes, or UAS-Sep2 (overexpression).

(J) Quantification of border cell migration in egg chambers with border cell clusters expressing UAS-MoesinRNAi, UAS-MoesinRNAi and UAS-Sep2 (overexpression), UAS-MoesinCA (constitutively active), or UAS-MoesinCA and UAS-Sep2RNAi. Scale bars: 5 μm in (A).

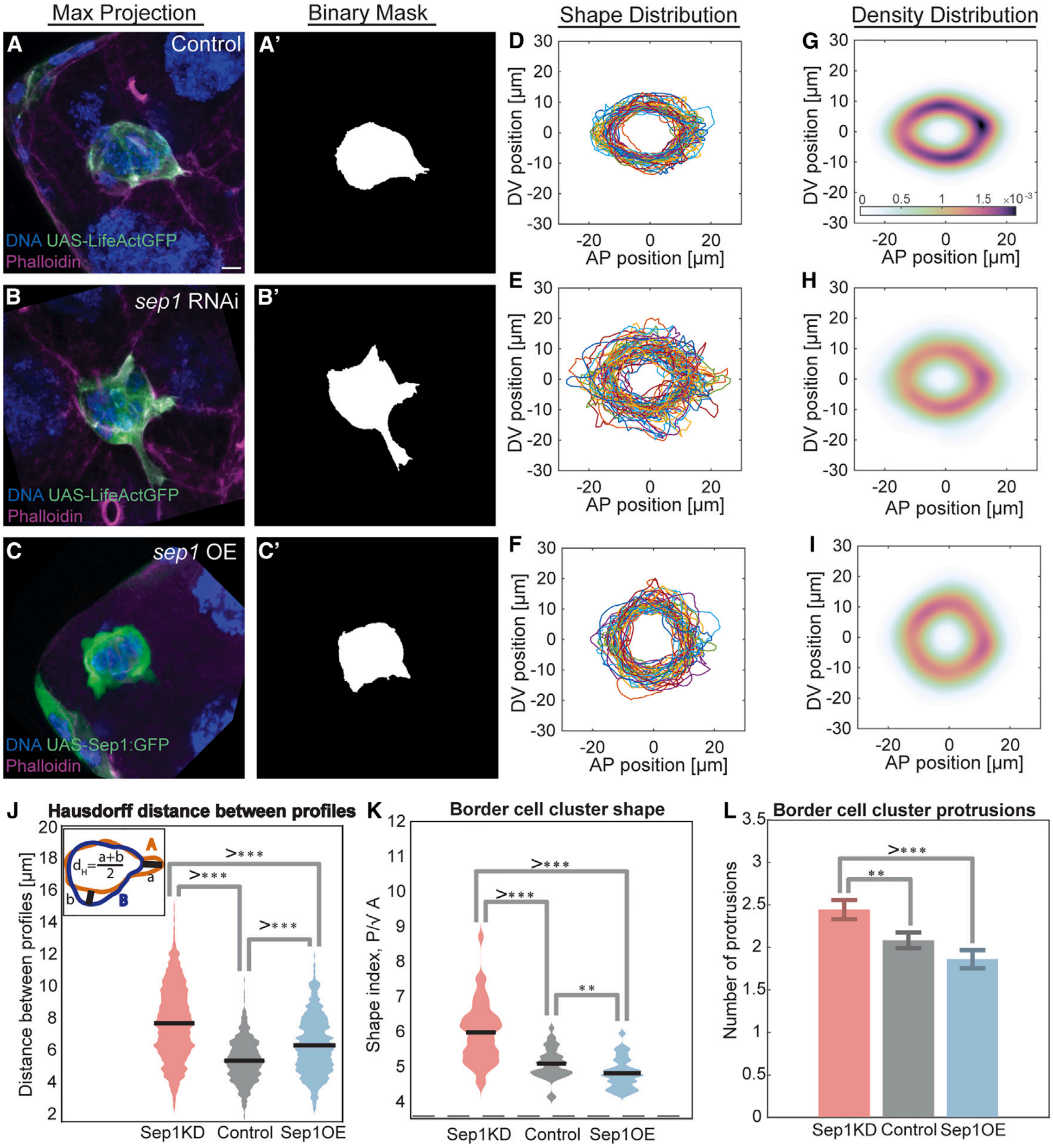

Figure 6. Septin knockdown and overexpression alter cluster shape

(A–C) Maximum intensity projections of border cell clusters expressing UAS-whiteRNAi (control) (A), UAS-Sep1RNAi (B), or UAS-Sep1:GFP (overexpression) (C). (A and B) Images labeled with UAS-LifeActGFP, Hoechst (blue), and Phalloidin (magenta). (C) Image labeled with UAS-Sep1:GFP, Hoechst (blue), and Phalloidin (magenta). (A′–C′) Binary masks of each cluster in (A)–(C).

(D–F) Overlapping outlines of all clusters analyzed. (D) is control, (E) is septin knockdown, and (F) is septin overexpression. Axes are of anterior-posterior (AP) and dorsal-ventral (DV) position.

(G–I) Density distribution plots of each genotype from (A)–(C) using a Gaussian kernel density estimation. Density correlates with the color scale.

(J) Dot plot of the Hausdorff distance between each genotype. Inset shows the calculation of Hausdorff distance as (a + b)/2.

(K) Dot plot of the border cell cluster shape of each genotype. Shape index represents the perimeter divided by the square root of the area for each cluster.

(L) Bar graph of the protrusion number for each genotype.

(J–L) $^{**}p < 0.01$ and $^{***}p < 0.001$ when analyzed by a Kolmogorov-Smirnov test (J and K) or a one-sided t test (L). Middle bars show means (J and K). Error bars show standard error (L). n = 36 for control, 45 for septin knockdown, and 36 for septin overexpression. Scale bars: 5 μm in (A).

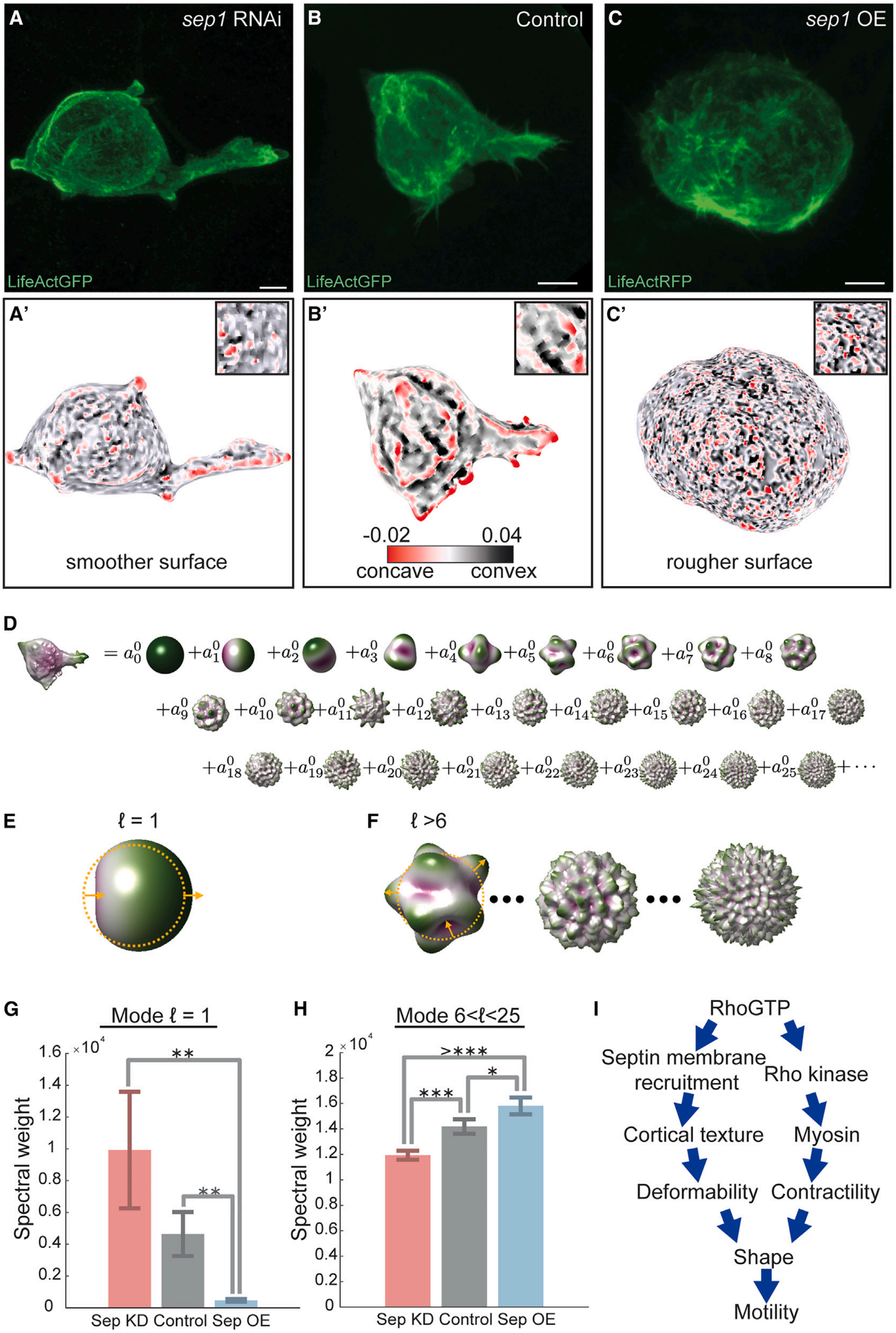

Figure 7. Septin knockdown and overexpression alter surface geometry

(A–C) Maximum intensity projection images of border cell clusters imaged by Airyscan after septin knockdown (A), control (B), or septin overexpression (C) and labeled by UAS-LifeActGFP (A and B) or UAS-LifeActRFP (C). (A′–C′) 3D curvature models of the surfaces of border cell clusters shown in (A)–(C) generated by a

(legend continued on next page)

S6A–S6O). We then overlaid the shapes to reveal the distributions in control (Figure 6D), septin knockdown (Figure 6E), and septin overexpression (Figure 6F). Control clusters had similar shapes (Figure 6D), whereas septin knockdown cluster shapes were more variable (Figure 6E). Compared with the control shape distribution, this distribution is more chaotic, with protrusions appearing in all orientations (Figures S6A–S6J). Septin overexpressing clusters also show more variability compared with controls (Figure 6F).

Another way to illustrate this variability is to display probability density distributions, which show that control clusters (Figure 6G) exhibit a more stereotyped set of shapes compared with the septin knockdown (Figure 6H). Clusters overexpressing septin likewise show more diffuse density distributions (Figure 6I). These clusters are rounder and less protrusive than controls, but some were skewed vertically and some horizontally relative to the direction of migration, increasing the overall variability and decreasing the density. To quantify the variability in cluster shapes, we calculated the Hausdorff distances as a measure of how far apart different curves (in this case the cluster perimeters) are from one another (Figure 6J; see supplemental information). Septin knockdown or overexpression results in larger and more variable Hausdorff distances compared with the control (Figure 6J), confirming that the shapes are more variable.

To quantify differences in shape, we measured the perimeter and divided it by the square root of the area to calculate a commonly used shape index.[64] While a perfect circle minimizes the shape index at value of $\sim$3.5 (dashed line at bottom of Figure 6K), protrusions or irregular surfaces will register higher values. Septin knockdown clusters deviated the most from a circle while septin overexpressing clusters were significantly rounder than controls (Figure 6K). We then defined an objective method for counting protrusions based on the amount of extension from a reference circle (see supplemental information). Septin knockdown caused significantly more protrusions than control clusters, which in turn produced more protrusions than clusters overexpressing septin (Figure 6L). We conclude that clusters with altered septin expression show a greater variability in shape compared with control clusters, but knockdown causes excess protrusions while overexpression produces rounder clusters.

Septin knockdown and overexpression alter surface texture

When septin protein is added to the outside of giant unilamellar lipid vesicles *in vitro*, it is sufficient to deform the sphere and cause projections,[65] so septins can act directly on membranes to reshape them. Septins are also known to induce membrane curvature in cells.[27] To describe membrane curvature in border cell clusters and determine whether septin knockdown or overexpression altered curvature, we took advantage of a MATLAB toolbox for tissue cartography called ImSAnE (image surface analysis environment).[66] This allowed us to generate 3D models of the cluster surface from high-resolution Airyscan images. We noticed that septin knockdown clusters exhibited an overall smoother texture (Figures 7A and 7A′) compared with control clusters (Figures 7B and 7B′), with fewer sharp features, whereas clusters overexpressing septin had a rougher texture with more numerous and smaller domains of steep, positive and negative curvature (Figures 7C and 7C′).

To quantify these differences, we performed a spectral decomposition of the shapes using a sphere as a frame of reference[67,68] (see supplemental information). This analysis describes a complex 3D object such as a border cell cluster as a sum of contributions of component shapes (Figure 7D), which are each weighted in the sum. The first component (which carries a weight A_1) measures deviations from sphericity at the largest possible scale—the cluster diameter. This component therefore describes an asymmetric shape with a single protrusion (with respect to a suitably defined centroid as described in the supplemental information) (Figure 7D). Higher-degree spectral components measure the contributions of shapes with finer-scale surface roughness (Figures 7D–7F). We found that the septin knockdown clusters, and to a lesser degree controls, are best described by heavily weighting the contribution of the first component and thus have a higher spectral weight in the first degree (Figure 7G), whereas the shapes of clusters overexpressing septin are best described by heavily weighting the higher-degree components (shown in Figure 7H for weights A_{7-25}).

With increasing septin expression, the higher-degree components contribute more to cluster shapes (Figures S7A and S7B), demonstrating that higher septin expression results in a fine-scale roughness. As our spectral analysis used LifeAct as a membrane marker, we validated our conclusions with the membrane marker PLCδ. We performed a spectral decomposition of control border cell clusters expressing both UAS-PLCδGFP and UAS-LifeActRFP and compared their spectral weights in the first degree and in higher modes. Using either PLCδGFP or LifeActRFP as a membrane marker yielded similar results in both low and high modes (Figures S7C and S7D). PLCδ and LifeAct also colocalized (Figure S7E). Spectral decomposition analysis of clusters segmented using UAS-PLCδGFP confirmed that septin knockdown clusters are best described by more heavily weighting lower modes compared with controls (Figures S7F and S7G).

Together, the analyses of cluster geometry suggest that the fine-scale smoothness caused by septin knockdown results in

---

tissue cartography tool, ImSAnE (image surface analysis environment). Insets are zooms. Concave and convex surfaces are denoted by a black to red color scheme.

(D–F) Spectral decomposition of 3D surface shape demonstrates that protrusivity decreases with septin expression, while surface roughness increases with septin expression. (D) The border cell cluster is a summation of component shapes of different weights. (E) The $\ell = 1$ spectral component measures “protrusivity,” or how much one side of the surface protrudes relative to the other with respect to a centroid found by mean curvature flow (see supplemental information for details). (F) Higher-degree spectral components (sketched for three surfaces $\ell > 6$) measure finer-scale surface roughness.

(G and H) (G) Septin expression is inversely correlated with protrusivity.

(H) Septin expression is correlated with greater surface roughness. (G and H) Error bars represent standard error. n = 4 for control, 10 for knockdown, and 3 for overexpression. $^*p < 0.05$, $^{**}p < 0.01$, and $^{***}p < 0.001$ when analyzed by one-sided t tests.

(I) Model for the independent functions of myosin and septin downstream of active Rho. Scale bars: 5 μm in (A), (B′), and (B).

more variability in cluster shape, more large-scale protrusions, and an overall more asymmetric shape. Conversely, septin overexpression causes fine-scale roughness that results in an overall more spherical and symmetrical cluster shape. While smoothness might naively be taken as an indication of rigidity, these findings suggest that the membrane is more rigid and less deformable when corrugated by increasing septin, akin to how fine-scale undulations in cardboard prevent bending at larger scales (see discussion).

DISCUSSION

Key open questions in the septin field include how the *in vitro* properties of septins relate to their *in vivo* functions, especially in multicellular organisms, how alterations in septin expression levels affect their functions, and how septins are regulated *in vivo*. Here, we address these questions using the border cell model of collective, confined, *in vivo* migration. We show that active Rho recruits septins to the plasma membrane, independently of Rok or myosin (Figure 7I). At the membrane, septin polymers tune surface properties including texture and deformability. Septin-mediated mechanical properties combine with myosin-mediated contractility to support appropriate protrusion and restrict inappropriate protrusion, thereby promoting collective migration through the confined 3D environment of the egg chamber (Figure 7I).

Border cell migration is a well-studied example of *in vivo* collective cell migration where the roles of Rho GTPases[24,61] and myosin[18,22,23,50,51] have been extensively explored. To date, myosin has been the only Rho effector identified in these cells. Here, we show that active Rho recruits septins to the plasma membrane where they colocalize dynamically with myosin. The results reported here may offer an explanation for earlier observations in cultured cells where active Rho modulates the mechanical strength of the cell cortex, independent of its activation of actomyosin contractility.[69] The molecules and mechanism were unidentified, but the current work suggests that septins could be the missing Rho effectors that modulate cortical mechanics.

The functions described here are consistent with and illustrate the significance of the activities of septins that have been described *in vitro*. For example, septins directly bind lipids and can deform giant unilamellar vesicles[65] and induce spikes.[70] Septins can also dramatically remodel 2D lipid bilayers into 3D structures.[71] Membrane recruitment also promotes septin polymerization by increasing the local septin protein concentration.[72] Here, we report the *in vivo* functional significance of septin membrane recruitment by showing that septin membrane recruitment is sufficient to rescue border cell migration defects due to RhoDN.

Alterations in septin expression levels occur in numerous human diseases.[33–35,73–75] However, the precise consequences of altered septin expression levels are not well understood and difficult to tease out. We show that either increasing or decreasing the level of septin expression alters cluster shape and impairs motility. We propose that the expression levels determine the abundance of membrane associated septin filaments, which in turn affects the deformability of the cell surface. Fewer cortical septin filaments cause a more flexible cortex, permissive for more but less functional protrusions. By contrast, increasing septin filaments produces a surface that is more difficult to deform at the scale of functional protrusions. Interestingly, this effect on large-scale protrusions likely results from the effects of septins on fine-scale roughness versus smoothness of the cell surface in a somewhat surprising way. The rough texture of the surfaces of clusters overexpressing septins may function like the corrugations in reinforced cardboard where fine-scale roughness makes the material more rigid and inhibits larger scale deformation. Thus, septin overexpression causes the overall cluster shape to be more spherical, whereas the fine-scale smoothness of septin knockdown clusters renders the surface more deformable and thus excessively protrusive.

We became interested in possible roles for septins in border cell migration based on differential expression. In a microarray analysis, we detected a 1.6× increase in Sep1 mRNA in border cells compared with non-migratory follicle cells and a 1.8× decrease in *slbo* mutant border cells, which lack a transcription factor required for motility. Although neither Pnut nor Sep2 mRNA was similarly affected, the results here show that Sep1, Sep2, and Pnut depend upon one another. Therefore, upregulating one subunit is likely sufficient to recruit the others, drive polymerization, and increase the abundance of filaments.

Septins are required in a great diversity of cell types for many different behaviors. It is striking that the morphology of border cells lacking septin exhibits commonalities with septin knockdown phenotypes in some individually migrating cells including the distal tip cell and neuronal axons in *C. elegans,*[76] and mammalian T cells.[28] In these examples, as in border cells, septin knockdown caused extra and ectopic protrusions as well as impaired migration. However, while T cells and border cells both exhibit less rigid surfaces upon septin knockdown, T cells were reported to migrate more effectively in a confined environment,[28] whereas we found that border cells move less effectively. The T cell transwell migration assays were conducted *in vitro* using non-deformable pores. This is different from the *in vivo* environment, which is composed of deformable cells. When moving through small, non-deformable pores, the only way for a cell to squeeze through is for the cell to deform. Therefore, less septin allows for a more flexible cortex and easier transit. However *in vivo*, cells including border cells, often need to move by pushing substrate cells apart. Pushing requires tensile strength in the cortex. This is a plausible explanation for how septin knockdown impedes migration between cells *in vivo* while facilitating migration through rigid pore *in vitro*. It would be interesting to test septin knockdown T cells for movement through different environments such as transendothelial migration or movement within cell-dense tissues such as lymph nodes and the thymus.

Neuronal progenitors in the developing mammalian cerebral cortex migrate along radial glial fibers through a cell-dense environment by extending a long, leading process. Septin 14 or septin 4 knockdown causes the neuronal processes to be shorter and impairs migration.[29] Exactly what role septins play in this context is not yet clear. Furthermore, the effects of septin overexpression have not been analyzed in these contexts, but based on our findings, we would predict that overexpression would cause different changes to cell shapes and would also likely impair migration.

Our analysis shows that the precise level of septin expression can affect the domains of microcurvature in cells with increasing septin leading to less deformable membranes. We show that reduction or increase in septin expression produces opposite effects on cell surface properties and cell shape and that either impairs motility. Humans have a larger set of septin genes and proteins than *Drosophila*. By modulating not only the expression levels but the compositions of septin filaments, this larger set might allow for even greater diversity of membrane properties and thus more diverse and complex cell shapes and behaviors, in both normal and pathological conditions.

STAR★METHODS

Detailed methods are provided in the online version of this paper and include the following:

- KEY RESOURCES TABLE
- RESOURCE AVAILABILITY
    - ○ Lead contact
    - ○ Materials availability
    - ○ Data and code availability
- EXPERIMENTAL MODEL AND STUDY PARTICIPANT DETAILS
    - ○ Drosophila husbandry
    - ○ RNAi knockdown with Gal4 drivers
    - ○ Egg chamber dissection and immunostaining
    - ○ Fixed sample imaging and image processing
    - ○ Live imaging
    - ○ Tissue cartography and curvature 3D models
- QUANTIFICATIONS AND STATISTICAL ANALYSES
    - ○ Migration index quantification
    - ○ Pnut intensity quantifications
    - ○ Sep2::GFP intensity quantifications
    - ○ Sqh intensity quantifications
    - ○ Kymograph generation
    - ○ Colocalization quantifications
    - ○ Membrane to cytoplasmic ratio
    - ○ Cytoplasmic septin puncta count
    - ○ Geomstats analysis in Python
    - ○ Spectral power analysis
    - ○ Statistics and data presentation

SUPPLEMENTAL INFORMATION

Supplemental information can be found online at https://doi.org/10.1016/j.devcel.2023.05.017.

ACKNOWLEDGMENTS

We thank the entire Montell lab for discussions and feedback. We thank Miles Keats, Nick Keefer, Abraham Sontay, and Spencer Phillips for technical assistance, and Dillon Cislo for discussions on spectral analysis. Funding: this work was supported by NIH grant R01 GM073164 to D.J.M. and ACS grant PF-17-024-01-CSM to J.P.C., and N.P.M. was supported by the Helen Hay Whitney Foundation. This work was also supported in part by the National Science Foundation grant no. NSF PHY-1748958 to the Kavli Institute for Theoretical Physics. We thank the Developmental Studies Hybridoma Bank for providing antibodies and the Bloomington Drosophila Stock Center and the Vienna Drosophila Resource Center for providing fly stocks.

AUTHOR CONTRIBUTIONS

Experiments were designed by A.M.G., J.P.C., J.A.M., and D.J.M. Experiments were carried out by A.M.G. with contributions by J.P.C. J.A.M. and J.P.C. assisted with computer software and microscopy. Data analysis was performed by A.M.G. Geomstats analysis was performed by N.P.M., A.M., and N.M. Spectral power analysis was performed by N.P.M. This manuscript was prepared by A.M.G., J.P.C., J.A.M., N.P.M., and D.J.M.

DECLARATION OF INTERESTS

The authors declare no competing interests.

INCLUSION AND DIVERSITY

Some authors self-identify as a member of an underrepresented group. We acknowledge the exclusions and erasures of many Indigenous peoples, including those on whose lands the University of California, Santa Barbara is located, the villages and unceded territories of the Chumash people. We acknowledge the Chumash people, their Elders, both past and present, and also their future generations. Efforts for balanced, equitable, and gender-unbiased citing were made throughout the development of this manuscript.

Received: September 18, 2022
Revised: April 14, 2023
Accepted: May 25, 2023
Published: June 16, 2023

REFERENCES

1. SenGupta, S., Parent, C.A., and Bear, J.E. (2021). The principles of directed cell migration. Nat. Rev. Mol. Cell Biol. *22*, 529–547. https://doi.org/10.1038/s41580-021-00366-6.
2. Stuelten, C.H., Parent, C.A., and Montell, D.J. (2018). Cell motility in cancer invasion and metastasis: insights from simple model organisms. Nat. Rev. Cancer *18*, 296–312. https://doi.org/10.1038/nrc.2018.15.
3. Perez-Vale, K.Z., and Peifer, M. (2020). Orchestrating morphogenesis: building the body plan by cell shape changes and movements. Development *147*. https://doi.org/10.1242/dev.191049.
4. Yamada, K.M., and Sixt, M. (2019). Mechanisms of 3D cell migration. Nat. Rev. Mol. Cell Biol. *20*, 738–752. https://doi.org/10.1038/s41580-019-0172-9.
5. Ridley, A.J., Schwartz, M.A., Burridge, K., Firtel, R.A., Ginsberg, M.H., Borisy, G., Parsons, J.T., and Horwitz, A.R. (2003). Cell migration: integrating signals from front to back. Science *302*, 1704–1709. https://doi.org/10.1126/science.1092053.
6. Shellard, A., and Mayor, R. (2021). Collective durotaxis along a self-generated stiffness gradient in vivo. Nature *600*, 690–694. https://doi.org/10.1038/s41586-021-04210-x.
7. Haeger, A., Wolf, K., Zegers, M.M., and Friedl, P. (2015). Collective cell migration: guidance principles and hierarchies. Trends Cell Biol. *25*, 556–566. https://doi.org/10.1016/j.tcb.2015.06.003.
8. Scarpa, E., and Mayor, R. (2016). Collective cell migration in development. J. Cell Biol. *212*, 143–155. https://doi.org/10.1083/jcb.201508047.
9. Mishra, A.K., Campanale, J.P., Mondo, J.A., and Montell, D.J. (2019). Cell interactions in collective cell migration. Development *146*, dev172056. https://doi.org/10.1242/dev.172056.
10. Friedl, P., and Gilmour, D. (2009). Collective cell migration in morphogenesis, regeneration and cancer. Nat. Rev. Mol. Cell Biol. *10*, 445–457. https://doi.org/10.1038/nrm2720.
11. Rørth, P. (2002). Initiating and guiding migration: lessons from border cells. Trends Cell Biol. *12*, 325–331. https://doi.org/10.1016/S0962-8924(02)02311-5.
12. Montell, D.J., Yoon, W.H., and Starz-Gaiano, M. (2012). Group choreography: mechanisms orchestrating the collective movement of border cells. Nat. Rev. Mol. Cell Biol. *13*, 631–645. https://doi.org/10.1038/nrm3433.

13. Prasad, M., Wang, X., He, L., and Montell, D.J. (2011). Border cell migration: a model system for live imaging and genetic analysis of collective cell movement. Methods Mol. Biol. *769*, 277–286. https://doi.org/10.1007/978-1-61779-207-6_19.

14. Montell, D.J. (2003). Border-cell migration: the race is on. Nat. Rev. Mol. Cell Biol. *4*, 13–24. https://doi.org/10.1038/nrm1006.

15. Seetharaman, S., and Etienne-Manneville, S. (2020). Cytoskeletal crosstalk in cell migration. Trends Cell Biol. *30*, 720–735. https://doi.org/10.1016/j.tcb.2020.06.004.

16. Zegers, M.M., and Friedl, P. (2014). Rho GTPases in collective cell migration. Small GTPases *5*, e28997. https://doi.org/10.4161/sgtp.28997.

17. Wang, H., Guo, X., Wang, X., Wang, X., and Chen, J. (2020). Supracellular actomyosin mediates cell-cell communication and shapes collective migratory morphology. iScience *23*, 101204. https://doi.org/10.1016/j.isci.2020.101204.

18. Zeledon, C., Sun, X., Plutoni, C., and Emery, G. (2019). The ArfGAP drongo promotes actomyosin contractility during collective cell migration by releasing myosin phosphatase from the trailing edge. Cell Rep. *28*, 3238–3248.e3. https://doi.org/10.1016/j.celrep.2019.08.044.

19. Plutoni, C., Keil, S., Zeledon, C., Delsin, L.E.A., Decelle, B., Roux, P.P., Carréno, S., and Emery, G. (2019). Misshapen coordinates protrusion restriction and actomyosin contractility during collective cell migration. Nat. Commun. *10*, 3940. https://doi.org/10.1038/s41467-019-11963-7.

20. Sawant, K., Chen, Y., Kotian, N., Preuss, K.M., and McDonald, J.A. (2018). Rap1 GTPase promotes coordinated collective cell migration in vivo. Mol. Biol. Cell *29*, 2656–2673. https://doi.org/10.1091/mbc.E17-12-0752.

21. Chang, Y.-C., Wu, J.-W., Hsieh, Y.-C., Huang, T.-H., Liao, Z.-M., Huang, Y.-S., Mondo, J.A., Montell, D., and Jang, A.C.-C. (2018). Rap1 negatively regulates the hippo pathway to polarize directional protrusions in collective cell migration. Cell Rep. *22*, 2160–2175. https://doi.org/10.1016/j.celrep.2018.01.080.

22. Mishra, A.K., Mondo, J.A., Campanale, J.P., and Montell, D.J. (2019). Coordination of protrusion dynamics within and between collectively migrating border cells by myosin II. Mol. Biol. Cell *30*, 2490–2502. https://doi.org/10.1091/mbc.E19-02-0124.

23. Combedazou, A., Choesmel-Cadamuro, V., Gay, G., Liu, J., Dupré, L., Ramel, D., and Wang, X. (2017). Myosin II governs collective cell migration behaviour downstream of guidance receptor signalling. J. Cell Sci. *130*, 97–103. https://doi.org/10.1242/jcs.179952.

24. Murphy, A.M., and Montell, D.J. (1996). Cell type-specific roles for Cdc42, Rac, and RhoL in Drosophila oogenesis. J. Cell Biol. *133*, 617–630. https://doi.org/10.1083/jcb.133.3.617.

25. Mostowy, S., and Cossart, P. (2012). Septins: the fourth component of the cytoskeleton. Nat. Rev. Mol. Cell Biol. *13*, 183–194. https://doi.org/10.1038/nrm3284.

26. Hartwell, L. (1971). Genetic control of the cell division cycle in yeast *1IV. Genes controlling bud emergence and cytokinesis. Exp. Cell Res. *69*, 265–276. https://doi.org/10.1016/0014-4827(71)90223-0.

27. Woods, B.L., and Gladfelter, A.S. (2021). The state of the septin cytoskeleton from assembly to function. Curr. Opin. Cell Biol. *68*, 105–112. https://doi.org/10.1016/j.ceb.2020.10.007.

28. Tooley, A.J., Gilden, J., Jacobelli, J., Beemiller, P., Trimble, W.S., Kinoshita, M., and Krummel, M.F. (2009). Amoeboid T lymphocytes require the septin cytoskeleton for cortical integrity and persistent motility. Nat. Cell Biol. *11*, 17–26. https://doi.org/10.1038/ncb1808.

29. Shinoda, T., Ito, H., Sudo, K., Iwamoto, I., Morishita, R., and Nagata, K. (2010). Septin 14 is involved in cortical neuronal migration via interaction with septin 4. Mol. Biol. Cell *21*, 1324–1334. https://doi.org/10.1091/mbc.e09-10-0869.

30. Oh, Y., and Bi, E. (2011). Septin structure and function in yeast and beyond. Trends Cell Biol. *21*, 141–148. https://doi.org/10.1016/j.tcb.2010.11.006.

31. Shindo, A., and Wallingford, J.B. (2014). PCP and septins compartmentalize cortical actomyosin to direct collective cell movement. Science *343*, 649–652. https://doi.org/10.1126/science.1243126.

32. Olguin-Olguin, A., Aalto, A., Maugis, B., Boquet-Pujadas, A., Hoffmann, D., Ermlich, L., Betz, T., Gov, N.S., Reichman-Fried, M., and Raz, E. (2021). Chemokine-biased robust self-organizing polarization of migrating cells in vivo. Proc. Natl. Acad. Sci. USA *118*, e2018480118. https://doi.org/10.1073/pnas.2018480118.

33. Hall, P.A., and Russell, S.E.H. (2004). The pathobiology of the septin gene family. J. Pathol. *204*, 489–505. https://doi.org/10.1002/path.1654.

34. Marttinen, M., Kurkinen, K.M., Soininen, H., Haapasalo, A., and Hiltunen, M. (2015). Synaptic dysfunction and septin protein family members in neurodegenerative diseases. Mol. Neurodegener. *10*, 16. https://doi.org/10.1186/s13024-015-0013-z.

35. Peterson, E.A., and Petty, E.M. (2010). Conquering the complex world of human septins: implications for health and disease. Clin. Genet. *77*, 511–524. https://doi.org/10.1111/j.1399-0004.2010.01392.x.

36. Saarikangas, J., and Barral, Y. (2011). The emerging functions of septins in metazoans. EMBO Rep. *12*, 1118–1126. https://doi.org/10.1038/embor.2011.193.

37. Field, C.M., al-Awar, O., Rosenblatt, J., Wong, M.L., Alberts, B., and Mitchison, T.J. (1996). A purified Drosophila septin complex forms filaments and exhibits GTPase activity. J. Cell Biol. *133*, 605–616. https://doi.org/10.1083/jcb.133.3.605.

38. Wang, X., Bo, J., Bridges, T., Dugan, K.D., Pan, T.C., Chodosh, L.A., and Montell, D.J. (2006). Analysis of cell migration using whole-genome expression profiling of migratory cells in the Drosophila ovary. Dev. Cell *10*, 483–495. https://doi.org/10.1016/j.devcel.2006.02.003.

39. Bridges, A.A., Jentzsch, M.S., Oakes, P.W., Occhipinti, P., and Gladfelter, A.S. (2016). Micron-scale plasma membrane curvature is recognized by the septin cytoskeleton. J. Cell Biol. *213*, 23–32. https://doi.org/10.1083/jcb.201512029.

40. Prasad, M., and Montell, D.J. (2007). Cellular and molecular mechanisms of border cell migration analyzed using time-lapse live-cell imaging. Dev. Cell *12*, 997–1005. https://doi.org/10.1016/j.devcel.2007.03.021.

41. Dolat, L., Hu, Q., and Spiliotis, E.T. (2014). Septin functions in organ system physiology and pathology. Biol. Chem. *395*, 123–141. https://doi.org/10.1515/hsz-2013-0233.

42. Akhmetova, K., Balasov, M., Svitin, A., Chesnokova, E., Renfrow, M., and Chesnokov, I. (2018). Phosphorylation of Pnut in the early stages of drosophila embryo development affects association of the septin complex with the membrane and is important for viability. G3 (Bethesda) *8*, 27–38. https://doi.org/10.1534/g3.117.300186.

43. Menon, M.B., Sawada, A., Chaturvedi, A., Mishra, P., Schuster-Gossler, K., Galla, M., Schambach, A., Gossler, A., Förster, R., Heuser, M., et al. (2014). Genetic deletion of Sept7 reveals a cell type-specific role of septins in microtubule destabilization for the completion of cytokinesis. PLoS Genet. *10*, e1004558. https://doi.org/10.1371/journal.pgen.1004558.

44. Xu, D., Liu, A., Wang, X., Chen, Y., Shen, Y., Tan, Z., and Qiu, M. (2018). Repression of Septin9 and Septin2 suppresses tumor growth of human glioblastoma cells. Cell Death Dis. *9*, 514. https://doi.org/10.1038/s41419-018-0547-4.

45. Fares, H., Peifer, M., and Pringle, J.R. (1995). Localization and possible functions of Drosophila septins. Mol. Biol. Cell *6*, 1843–1859.

46. Huijbregts, R.P.H., Svitin, A., Stinnett, M.W., Renfrow, M.B., and Chesnokov, I. (2009). Drosophila Orc6 facilitates GTPase activity and filament formation of the septin complex. Mol. Biol. Cell *20*, 270–281. https://doi.org/10.1091/mbc.E08-07-0754.

47. Caviston, J.P., Longtine, M., Pringle, J.R., and Bi, E. (2003). The role of Cdc42p GTPase-activating proteins in assembly of the septin ring in yeast. Mol. Biol. Cell *14*, 4051–4066. https://doi.org/10.1091/mbc.E03-04-0247.

48. Schneider, C., Grois, J., Renz, C., Gronemeyer, T., and Johnsson, N. (2013). Septin rings act as a template for myosin higher-order structures

and inhibit redundant polarity establishment. J. Cell Sci. *126*, 3390–3400. https://doi.org/10.1242/jcs.125302.

49. Joo, E., Surka, M.C., and Trimble, W.S. (2007). Mammalian Sept2 is required for scaffolding nonmuscle myosin II and its kinases. Dev. Cell *13*, 677–690. https://doi.org/10.1016/j.devcel.2007.09.001.
50. Majumder, P., Aranjuez, G., Amick, J., and McDonald, J.A. (2012). Par-1 controls myosin-II activity through myosin phosphatase to regulate border cell migration. Curr. Biol. *22*, 363–372. https://doi.org/10.1016/j.cub.2012.01.037.
51. Aranjuez, G., Burtscher, A., Sawant, K., Majumder, P., and McDonald, J.A. (2016). Dynamic myosin activation promotes collective morphology and migration by locally balancing oppositional forces from surrounding tissue. Mol. Biol. Cell *27*, 1898–1910. https://doi.org/10.1091/mbc.E15-10-0744.
52. Lippincott, J., and Li, R. (1998). Sequential assembly of myosin II, an IQGAP-like protein, and filamentous actin to a ring structure involved in budding yeast cytokinesis. J. Cell Biol. *140*, 355–366. https://doi.org/10.1083/jcb.140.2.355.
53. Ito, H., Iwamoto, I., Morishita, R., Nozawa, Y., Narumiya, S., Asano, T., and Nagata, K.-I. (2005). Possible role of Rho/Rhotekin signaling in mammalian septin organization. Oncogene *24*, 7064–7072. https://doi.org/10.1038/sj.onc.1208862.
54. Carim, S.C., Kechad, A., and Hickson, G.R.X. (2020). Animal cell cytokinesis: the rho-dependent actomyosin-Anilloseptin contractile ring as a membrane microdomain gathering, compressing, and sorting machine. Front. Cell Dev. Biol. *8*, 575226. https://doi.org/10.3389/fcell.2020.575226.
55. Pérez, P., Portales, E., and Santos, B. (2015). Rho4 interaction with exocyst and septins regulates cell separation in fission yeast. Microbiol. Reading Engl. *161*, 948–959. https://doi.org/10.1099/mic.0.000062.
56. Harmansa, S., Alborelli, I., Bieli, D., Caussinus, E., and Affolter, M. (2017). A nanobody-based toolset to investigate the role of protein localization and dispersal in Drosophila. eLife *6*, e22549. https://doi.org/10.7554/eLife.22549.
57. Miao, G., Guo, L., and Montell, D.J. (2022). Border cell polarity and collective migration require the spliceosome component Cactin. J. Cell Biol. *221*, e202202146. https://doi.org/10.1083/jcb.202202146.
58. Campanale, J.P., Mondo, J.A., and Montell, D.J. (2022). A Scribble/Cdep/Rac pathway regulates follower cell crawling and cluster cohesion during collective border cell migration. https://doi.org/10.1101/2022.01.04.474957.
59. Fulga, T.A., and Rørth, P. (2002). Invasive cell migration is initiated by guided growth of long cellular extensions. Nat. Cell Biol. *4*, 715–719. https://doi.org/10.1038/ncb848.
60. Cai, D., Chen, S.C., Prasad, M., He, L., Wang, X., Choesmel-Cadamuro, V., Sawyer, J.K., Danuser, G., and Montell, D.J. (2014). Mechanical feedback through E-cadherin promotes direction sensing during collective cell migration. Cell *157*, 1146–1159. https://doi.org/10.1016/j.cell.2014.03.045.
61. Colombié, N., Choesmel-Cadamuro, V., Series, J., Emery, G., Wang, X., and Ramel, D. (2017). Non-autonomous role of Cdc42 in cell-cell communication during collective migration. Dev. Biol. *423*, 12–18. https://doi.org/10.1016/j.ydbio.2017.01.018.
62. Ramel, D., Wang, X., Laflamme, C., Montell, D.J., and Emery, G. (2013). Rab11 regulates cell-cell communication during collective cell movements. Nat. Cell Biol. *15*, 317–324. https://doi.org/10.1038/ncb2681.
63. Dai, W., Guo, X., Cao, Y., Mondo, J.A., Campanale, J.P., Montell, B.J., Burrous, H., Streichan, S., Gov, N., Rappel, W.J., et al. (2020). Tissue topography steers migrating Drosophila border cells. Science *370*, 987–990. https://doi.org/10.1126/science.aaz4741.
64. Bi, D., Lopez, J.H., Schwarz, J.M., and Manning, M.L. (2015). A density-independent rigidity transition in biological tissues. Nat. Phys. *11*, 1074–1079. https://doi.org/10.1038/nphys3471.
65. Beber, A., Taveneau, C., Nania, M., Tsai, F.C., Di Cicco, A., Bassereau, P., Lévy, D., Cabral, J.T., Isambert, H., Mangenot, S., et al. (2019). Membrane reshaping by micrometric curvature sensitive septin filaments. Nat. Commun. *10*, 420. https://doi.org/10.1038/s41467-019-08344-5.
66. Heemskerk, I., and Streichan, S.J. (2015). Tissue cartography: compressing bio-image data by dimensional reduction. Nat. Methods *12*, 1139–1142. https://doi.org/10.1038/nmeth.3648.
67. Dalmasso, G., Musy, M., Niksic, M., Robert-Moreno, A., Badía-Careaga, C., Sanz-Ezquerro, J.J., and Sharpe, J. (2022). 4D reconstruction of murine developmental trajectories using spherical harmonics. Dev. Cell *57*, 2140–2150.e5. https://doi.org/10.1016/j.devcel.2022.08.005.
68. Mitchell, N.P., and Cislo, D.J. (2022). TubULAR: tracking deformations of dynamic tissues and interfaces in. https://doi.org/10.1101/2022.04.19.488840.
69. O'Connell, C.B., Wheatley, S.P., Ahmed, S., and Wang, Y.L. (1999). The small GTP-binding protein rho regulates cortical activities in cultured cells during division. J. Cell Biol. *144*, 305–313. https://doi.org/10.1083/jcb.144.2.305.
70. Tanaka-Takiguchi, Y., Kinoshita, M., and Takiguchi, K. (2009). Septin-mediated uniform bracing of phospholipid membranes. Curr. Biol. *19*, 140–145. https://doi.org/10.1016/j.cub.2008.12.030.
71. Vial, A., Taveneau, C., Costa, L., Chauvin, B., Nasrallah, H., Godefroy, C., Dosset, P., Isambert, H., Ngo, K.X., Mangenot, S., et al. (2021). Correlative AFM and fluorescence imaging demonstrate nanoscale membrane remodeling and ring-like and tubular structure formation by septins. Nanoscale *13*, 12484–12493. https://doi.org/10.1039/d1nr01978c.
72. Szuba, A., Bano, F., Castro-Linares, G., Iv, F., Mavrakis, M., Richter, R.P., Bertin, A., and Koenderink, G.H. (2021). Membrane binding controls ordered self-assembly of animal septins. eLife *10*, e63349. https://doi.org/10.7554/eLife.63349.
73. Hall, P.A., Jung, K., Hillan, K.J., and Russell, S.E.H. (2005). Expression profiling the human septin gene family. J. Pathol. *206*, 269–278. https://doi.org/10.1002/path.1789.
74. Wang, X., Fei, F., Qu, J., Li, C., Li, Y., and Zhang, S. (2018). The role of septin 7 in physiology and pathological disease: A systematic review of current status. J. Cell. Mol. Med. *22*, 3298–3307. https://doi.org/10.1111/jcmm.13623.
75. Montagna, C., Sagie, M., and Zechmeister, J. (2015). Mammalian septins in health and disease. RRBC *2015*, 59–72. https://doi.org/10.2147/RRBC.S59060.
76. Finger, F.P., Kopish, K.R., and White, J.G. (2003). A role for septins in cellular and axonal migration in C. elegans. Dev. Biol. *261*, 220–234. https://doi.org/10.1016/S0012-1606(03)00296-3.
77. Schindelin, J., Arganda-Carreras, I., Frise, E., Kaynig, V., Longair, M., Pietzsch, T., Preibisch, S., Rueden, C., Saalfeld, S., Schmid, B., et al. (2012). Fiji: an open-source platform for biological-image analysis. Nat. Methods *9*, 676–682. https://doi.org/10.1038/nmeth.2019.
78. Berg, S., Kutra, D., Kroeger, T., Straehle, C.N., Kausler, B.X., Haubold, C., Schiegg, M., Ales, J., Beier, T., Rudy, M., et al. (2019). ilastik: interactive machine learning for (bio)image analysis. Nat. Methods *16*, 1226–1232. https://doi.org/10.1038/s41592-019-0582-9.
79. Cignoni, P., Callieri, M., Corsini, M., Dellepiane, M., Ganovelli, F., and Ranzuglia, G. (2008). MeshLab: an Open-Source Mesh Processing Tool (The Eurographics Association). https://doi.org/10.2312/localchapterevents/italchap/italianchapconf2008/129-136.
80. Miolane, N., Guigui, N., Brigant, A.L., Mathe, J., Hou, B., Thanwerdas, Y., Heyder, S., Peltre, O., Koep, N., Zaatiti, H., et al. (2020). Geomstats: A python package for Riemannian geometry in machine learning. https://doi.org/10.48550/arXiv.2004.04667.
81. Kazhdan, M., Solomon, J., and Ben-Chen, M. (2012). Can mean-curvature flow be modified to be non-singular? Comput. Graphics Forum *31*, 1745–1754. https://doi.org/10.1111/j.1467-8659.2012.03179.x.

STAR★METHODS

KEY RESOURCES TABLE

REAGENT or RESOURCE	SOURCE	IDENTIFIER
Antibodies		
Monoclonal rat anti-Ecadherin (1:25 dilution)	Developmental Studies Hybridoma Bank	Cat# DCAD2; RRID: AB_528120
Monoclonal mouse anti-Peanut (1:25 dilution)	Developmental Studies Hybridoma Bank	Cat# 4C9H4 anti-peanut; RRID: AB_528429
Monoclonal mouse anti-Singed (Fascin) (1:50 dilution)	Developmental Studies Hybridoma Bank	Cat# sn 7c; RRID: AB_52823
Polyclonal rabbit anti-GFP (1:300 dilution)	ThermoFisher	Cat# A-11122; RRID: AB_221569
Polyclonal rabbit anti-mCherry (1:500 dilution)	Novusbio	Cat# NBP2-25157SS; RRID: AB_2753204
Chemicals, peptides, and recombinant proteins		
Hoechst 33342	Sigma-Aldrich	Cat# 14533
Phalloidin Atto647N	Sigma-Aldrich	Cat# 65906
TritonX-100	Sigmal-Aldrich	Cat# T8787
Schneider's Drosophila Medium	Gibco	Cat# 21720
Phosphate Buffered Saline (10x, pH 7.4)	Quality Biological	Cat# 119-069-131
Paraformaldehyde, 16% solution	Electron Microscopy Sciences	Cat# 15710
Vectasheild antifade mounting medium	Vector Laboratories	Cat# H-1000
Antibiotic-Antimycotic (100X)	ThermoFisher Scientific	Cat# 15240062
Insulin (bovine pancreas)	Sigmal-Aldrich	Cat# I1882
Experimental models: Organisms/strains		
c306Gal4;UAS-LifeActGFP;Gal80ts	Denise Montell Lab Stock, University of California Santa Barbara	N/A
y[1] w[*]; P{w[+mC]=Septin2-GFP.SG}3	Bloomington Drosophila Stock Center	Cat# BDSC_26257
hsFLP;AyGal4-25b,UASredstingerNLS	Denise Montell Lab Stock, University of California Santa Barbara	N/A
c306Gal4;sqh::sqh-mcherry/CyO	Denise Montell Lab Stock, University of California Santa Barbara	N/A
sqh::sqh-mcherry/(CyO);MKRS/TM6B	Denise Montell Lab Stock, University of California Santa Barbara	N/A
D. melanogaster y[1] v[1]; P{y[+t7.7] v[+t1.8]=TRiP.HMS00017}attP2	Bloomington Drosophila Stock Center	Cat# BDSC_33623
w[1118]; P{GD8198}v17344	Vienna Drosophila Resource Center	Cat# VDRC_17344
w1118; P{GD11240}v26413	Vienna Drosophila Resource Center	Cat# VDRC_26413
w1118 P{GD1512}v11791	Vienna Drosophila Resource Center	Cat# VDRC 11791
w[1118]; P{w[+mC]=UAS-Cdc42.V12}LL1	Bloomington Drosophila Stock Center	Cat# BDSC_4854
w[*]; P{w[+mC]=UAS-Cdc42.N17}3	Bloomington Drosophila Stock Center	Cat# BDSC_6288
P{VSH330192}attP40	Vienna Drosophila Resource Center	Cat# VDRC_330192
P{KK108698}VIE-260B	Vienna Drosophila Resource Center	Cat# VDRC_100794
w[*]; P{w[+mC]=UASp-Septin1.GFP}3	Bloomington Drosophila Stock Center	Cat# BDSC_51346
w[*]; P{w[+mC]=UASp-Septin2.O}18A/CyO	Bloomington Drosophila Stock Center	Cat# BDSC_91012
w1118; P{GD1695}v7917/TM3	Vienna Drosophila Resource Center	Cat# VDRC_7917
w[*]; P{w[+mC]=UAS-Rho1.V14}5.1/CyO	Bloomington Drosophila Stock Center	Cat# BDSC_7330
w[*]; P{w[+mC]=UAS-Rho1.V14}2.1/TM6	Bloomington Drosophila Stock Center	Cat# BDSC_8144
P{w[+mC]=UAS-Rho1.N19}1.3, w[*]	Bloomington Drosophila Stock Center	Cat# BDSC_#7327
hsFLP;AyGal4, UAS-GFP;MKRS	Denise Montell Lab Stock, University of California Santa Barbara	N/A

(*Continued on next page*)

Continued

REAGENT or RESOURCE	SOURCE	IDENTIFIER
w[*]; Septin2[1]/TM6B, Tb[1]	Bloomington Drosophila Stock Center	Cat# BDSC_91002
w[*]; Septin2[2]/TM6B, Tb[1]	Bloomington Drosophila Stock Center	Cat# BDSC_91003
yw, hsFLP;;FRT82B, ubiRFPnls	Denise Montell Lab Stock, University of California Santa Barbara	N/A
w[*]; P{w[+mC]=UASp-sqh.A20A21}3	Bloomington Drosophila Stock Center	Cat# BDSC_64114
w[*]; P{w[+mC]=UASp-sqh.E20E21}3	Bloomington Drosophila Stock Center	Cat# BDSC_64411
P{VSH330299}attP40	Vienna Drosophila Resource Center	Cat# VDRC_330299
y[1] w[*]; P{w[+mC]=UAS-Rok.CAT}7.1	Bloomington Drosophila Stock Center	Cat# BDSC_6668
w[*]; P{w[+mC]=UAS-Rok.CAT-KG}2B1	Bloomington Drosophila Stock Center	Cat# BDSC_6670
y[1] sc[*] v[1] sev[21]; P{y[+t7.7] v[+t1.8]=TRiP.GL00209}attP2	Bloomington Drosophila Stock Center	Cat# BDSC_35305
w[1118]; P{w[+mC]=UAS-Moe.T559D.MYC}2	Bloomington Drosophila Stock Center	Cat# BDSC_8630
w[1118]; P{w[+mC]=UAS-Moe.IR.327-775}3	Bloomington Drosophila Stock Center	Cat# BDSC_8629
w[1118]; P{w[+mC]=UAS-Moe.IR.327-775}3	Bloomington Drosophila Stock Center	Cat# BDSC_32904
w[*]; Kr[If-1]/CyO; M{w[+mC]=lexAop-UAS-morphotrap.int.mCh}ZH-86Fb	Bloomington Drosophila Stock Center	Cat# BDSC_68172
c306Gal4, Gal80ts;; UASPLCdeltaGFP/TM3,Ser	Denise Montell Lab Stock, University of California Santa Barbara	N/A
Software and algorithms		
ImageJ2 (FIJI)	Schindelin et al.[77]	fiji.sc
Adobe Illustrator 2022	Adobe	adobe.com
Imaris 9	Bitplane	imaris.oxinst.com
Prism 9	Graph Pad	graphpad.com
Ilastik	Berg et al.[78]	ilastik.org
MeshLab	Cignoni et al.[79]	meshlab.net
MATLAB	MathWorks	mathworks.com
Python	Python Software Foundation	python.org
Graphic	Apple	graphic.com
Zen	Zeiss	zeiss.com/microscopy
Geomstats	Miolane et al.[80]	geomstats.github.io

RESOURCE AVAILABILITY

Lead contact

Further information and requests for resources and reagents should be directed to and will be fulfilled by the lead contact, Denise Montell (dmontell@ucsb.edu).

Materials availability

Drosophila lines and other reagents generated in this study will be available upon request.

Data and code availability

- Data including all raw image files in this study will be made available upon request.
- All original code has been deposited in Github repository AllisonGabbert/SeptinManuscriptData and is publicly available as of the date of publication.
- Any additional information required to reanalyze the data reported in this paper is available from the lead contact upon request.

EXPERIMENTAL MODEL AND STUDY PARTICIPANT DETAILS

Drosophila husbandry

Fly strains were raised in vials containing a standard cornmeal-yeast food (https://bdsc.indiana.edu/information/recipes/molassesfood.html) which contains 163g yellow cornmeal, 33g dried yeast, 200mL molasses and 16g agar with 2.66L water. All flies were raised in vials containing 5mL fly food.

Method Details

RNAi knockdown with Gal4 drivers

A detailed list of all fly strains used in this study and their source can be found in the key resources table. Genotypes for every figure panel can be found in Table S1. 2-4 day-old females were kept in 29°C for 3 days and transferred to a vial with dry yeast each day until dissection. FLPout clones were first heat-shocked for 1 h at 37°C to induce clones, kept at room temperature for 8 h, heat-shocked again at 37°C for 1 h, and then kept at 29°C for 3 days with dry yeast until dissection.

Egg chamber dissection and immunostaining

Adult female ovaries were dissected in Schneider's Drosophila medium (Thermo Fisher Scientific, Waltham, MA; 21720) with 20% fetal bovine serum. Ovarioles containing egg chambers of the desired stages were pulled out of the muscle sheath with #55 forceps. For fixed sample staining, ovarioles were then fixed for 15 min in 4% paraformaldehyde. After fixation, ovarioles were washed with PBS/0.1% Triton X-100 (PBST) or PBS/0.4% Triton X-100 (PBST), and then incubated with primary antibodies overnight at 4 °C. The following day, ovarioles were washed with PBST before incubation in secondary antibodies and Hoechst overnight at 4 °C. The following day, ovarioles were again washed with PBST. Samples were stored in VECTASHIELD (Vector Laboratories, Burlingame, CA) at 4 °C before mounting.

The following antibodies and dyes were used in this study: Hoechst (1:1000, sigma-aldrich), rat anti-E-cadherin (1:25, DCAD2, DSHB), mouse anti-Singed (1:50, DSHB), mouse anti-Pnut (1:50, 4C9H4, DSHB), rabbit anti-GFP (1:300, lifetech), rabbit anti-mCherry (1:500, novusbio), Alexa 488, 568, 647 (1:200, lifetech), phalloidin 647 (1:200, sigma-aldrich).

Fixed sample imaging and image processing

Samples were mounted on a glass slide in VECTASHIELD. Images were taken on a Zeiss LSM 800 confocal microscope, using a 20× 1.2 N.A. objective, 40×1.4 N.A. water objective, or 63x 0.8 NA water and oil objective.

Live imaging

Ovaries were dissected in Schneider's Drosophila medium (Thermo Fisher Scientific, Waltham, MA) with 20% fetal bovine serum. Individual ovarioles were carefully pulled out. The egg chambers were collected in a 0.6 mL tube and washed with dissecting medium twice, then added to 100 uL dissecting medium with insulin (100 ug/uL) and 1% low melt agarose. 100 uL medium with the egg chambers then were mounted on a 50mmLumox dish. Time-lapse imaging was performed using a 20×1.2N.A. objective or 40×1.1 NA water immersion objective lens.

Tissue cartography and curvature 3D models

We imaged migrating border cell clusters through high-resolution airyscan imaging. These images were imported into Ilastik,[78] an open source software for segmenting cells using machine learning. We used this to define the surface of the border cell cluster, and exported this file as a.h5 file. This.h5 file was imported into meshlab to clean up the mesh as well as generate a file that can be analyzed using ImSAnE (Image Surface Analysis Environment). MeshLab version used was MeshLab_64bit v1.3.3.[79] Mesh construction was done by: 1) importing the cell surface; 2) Filters -> Sampling -> Poisson disc sampling. Base mesh subsampling option must be checked. Number of samples used was 15,000; 3) Filters - > Normals, Curvature and Orientation -> computing 5ormal for point sets; 4) Filters -> Remeshing, Simplification and Reconstruction -> surface reconstruction: poisson. The reconstructed surface is then exported as a PLY file with the flags and normal data included. The PLY file was analyzed using ImSAnE, details provided in the reference above as well as comments within the example scripts provided by the authors in their GitHub [https://github.com/idse/imsane]. Specifically we modified the example script TutorialIlastikDetectorSpherelikeFitter.m running on Matlab_R2019a.

QUANTIFICATIONS AND STATISTICAL ANALYSES

Migration index quantification

To measure the migration index of border cells in different conditions, border cell cluster positions were scored in fixed stage 10 egg chambers by eye. The position of the border cell clusters were assigned to categories of 0%, 1-25%, 26-50%, 51-75%, or 76-100% based on their distance from the anterior of the egg chamber to the oocyte (Figures 2H, 5H–5J, and S4O).

Pnut intensity quantifications

For quantification of Pnut intensity, 20x, 40x, or 63x images of Pnut channel were measured in FIJI.[77] When measuring Pnut intensity in follicle cells or border cells, a single slice in the center of the z stack was measured that clearly showed the cells of interest. About 3-5 follicle cells or one border cell were measured when comparing clonal cells to adjacent non-clones (Figures 3A–3K and 4I–4N). All quantifications use raw integrated density normalized to area.

Sep2::GFP intensity quantifications

For quantification of Sep2::GFP intensity, samples were probed with anti-GFP antibody. 20x images of the GFP channel were measured in FIJI. When measuring Sep2::GFP intensity in follicle cells, a single slice in the center of the z stack was measured that clearly showed the cells of interest. About 3-5 follicle cells were measured when comparing UAS-RNAi expressing cells to control cells (Figure 3L). All quantifications use raw integrated density normalized to area.

Sqh intensity quantifications

For quantification of Sqh intensity, 20x, 40x, or 63x images of Sqh channel were measured in FIJI. When measuring Sqh intensity in follicle cells or border cells, a single slice in the center of the z stack was measured that clearly showed the cells of interest. About 3-5 follicle cells or one border cell were measured when comparing clonal cells to adjacent non-clones (Figures 4O–4T). All quantifications use raw integrated density normalized to area.

Kymograph generation

To generate the kymograph of dynamic Sqh::mCherry and Sep2::GFP signal, a line was drawn along the periphery of one side of the border cell cluster at a single z-slice in the center of the cluster for multiple timepoints. Kymograph was generated using FIJI KymographBuilder function (FIJI function: Plugins> Kymograph > KymographBuilder).

Colocalization quantifications

For colocalization quantifications in Figures S3C, S4S, and S6C, high-resolution Airyscan z-stack images of the border cell cluster were taken at 63x magnification with the 0.8 NA oil objective. For colocalization quantifications in Figure 5G, z-stack images of the border cell cluster were taken at 63x magnification with the 0.8 NA water objective. A single slice in the center of the z-stack was selected. A ROI was drawn to outline the cluster and background was subtracted. Colocalization of two channels within the ROI was measured using FIJI Coloc2 function (FIJI function: Analyze > Colocalization Analysis > Coloc 2). Pearson's correlation, r was used as the readout of colocalization.

Membrane to cytoplasmic ratio

To quantify the membrane to cytoplasmic ratio across nurse cell to border cell interfaces and border cell to border cell interfaces, z-stack images of the border cell cluster were taken at 63x magnification. A single slice in the center of the z-stack was selected. A line of width 25um was drawn across a membrane in clear view and intensity plot profiles were generated from the PLCδGFP and Pnut channels. The maximum intensity of the PLCδGFP channel was used as a marker for the membrane location and the first and last 20% of the intensity plots were categorized as cytoplasmic signal. The membrane to cytoplasmic ratio of Pnut was calculated by taking a ratio of Pnut intensity at the membrane location to the average of the sum of the cytoplasmic signal (Figures 5D and 5E).

Cytoplasmic septin puncta count

Z-stack images of border cell clusters were taken at 63x magnification and processed in Imaris Image analysis software. LifeActGFP and Pnut channels were used for this analysis. Gaussian smooth filter and background subtraction were applied to both channels. LifeActGFP channel was used to create a surface and then a distance transformation inside the surface was applied and made into a second surface. A mask was applied to convert any voxels outside of this surface to the value zero. A new surface was made from this mask. Using the spots module, spots in the Pnut channel were marked. Spots were categorized as close to or far from the third surface and only spots close to the surface were counted.

Geomstats analysis in Python

We plotted the shapes of each genotype using a software package in Python called Geomstats[80] to project each cluster shape onto the manifold of discrete curves. On the manifold of discrete curves, each point represents a different cluster shape. Thus, when we "projected" a cluster to the manifold, we are identifying which point on the manifold matches the shape of that cluster. We oriented all clusters so that the direction of motion was facing right. Shape indices were calculated by measuring the perimeter of each cluster (segmented as a maximum intensity projection) and dividing it by the square root of the area of that shape. To count protrusions, we identified stable maxima that are at least a distance R away from the centroid of the segmented border cell cluster and have a peak that is at least 0.3*R larger than the surrounding data to avoid overcounting. Here, we set R to equal the radius of a circle whose area is equal to the cluster under consideration. To measure Hausdorff distance between curves, we first collected all aligned curves outlining the border cell clusters, resampled them at 100 approximately equally spaced points, and expressed the positions of these points in physical units relative to the center of the cluster. For each pair of curves A and B within a given genotype, we then found the Hausdorff distance d(A,B) which is the maximum distance of any point in curve A from its closest point in B. The measurement was then symmetrized: 0.5*(d(A,B) + d(B, A)) for statistical analysis because the measurement of d(A,B) is not independent of d(B,A). We performed an all-to-all comparison within each category (WT, KD, OE) to build up a distribution. This gave N*(N-1)/2 symmetrized distances between pairs of curves (Figures 6D–6L and S6).

Spectral power analysis

To quantify the change in surface geometry in septin knockdowns and overexpression, we decomposed each cell cluster's surface profile into spherical harmonics using methods published by Mitchell and Cislo.[68] This measures the amount of surface deformation as a function of spatial scale, separating slow, long-wavelength variations in protrusion/ingression from short-wavelength roughness.

This procedure is analogous to taking a Fourier transform, in which a signal is decomposed into components which vary in their wavelength. To facilitate comparison across cells and across conditions, we conformally mapped each cell to a sphere[81] and defined a field on this sphere which indicates the extent of radial protrusion or ingression.

In detail, after acquiring each cell surface as a triangulated mesh, we conformally mapped a given cell's mesh to a spherical surface via mean curvature flow according to Kazhdan et al., resulting in a sphere of radius R centered at $\mathbf{r_0}$. Let us denote this conformal map f. This mapping enabled comparison across samples and across genotypes. We found the original distance of all surface vertices from the center r_0 (defined via conformal mean curvature flow) and subtracted R, which is the mapped radial distance from $\mathbf{r_0}$. This gave us a measure of how much the surface is extended beyond R or retracted from R at each point on the mesh. This defined a 'radial' surface profile δr, which can be expressed either as a function $\delta r(\mathbf{x})$ of position on the cell surface, or as a function $\delta r(f(\mathbf{x}))$ of position on the mapped sphere found by mean curvature flow. Scalar field patterns on the sphere can be compared directly across samples. Therefore, we decomposed the scalar field defined on the mapped (spherical) surface into spherical harmonics. Spherical harmonics Y_ℓ^m are a set of functions that can reproduce the original field when multiplied by appropriate spectral weights a_ℓ^m and summed together:

$$\delta r(\mathbf{x}) = \sum_{\ell=0}^{\infty} \sum_{m=-\ell}^{\ell} a_\ell^m Y_\ell^m$$

More formally, they are eigenmodes of the Laplace-Beltrami operator defined on the sphere. The inner product between a given eigenmode and the measured radial surface profile field δr defines the spectral weight at that spatial scale. We then plotted these weights as a function of index ℓ. Weights of different spherical harmonics Y_ℓ^m with identical index ℓ are summed together in each bin, since they represent similar wavelengths of variation along the surface:

$$A_\ell \equiv \sum_{m=-\ell}^{\ell} |a_\ell^m|$$

We took the absolute value of the weights in the sum. We then plotted A_ℓ as a function of the degree ℓ.

Comparing the lowest anisotropic component $\ell = 1$ across samples showed a significant trend, with spectral weight anti-correlated with septin expression. This component has higher weight when one side of the cell protrudes relative to the other. Higher-degree components measure short-wavelength roughness of the surface, and most high order modes are individually correlated with septin expression. Summing many modes together resulted in significant correlation with septin expression, and this result is insensitive to the lower or upper bound on ℓ included in the sum (Figures 7D–7H, S7A, S7B, S7D, and S7E).

Statistics and data presentation

Standard statistical tests were performed using Graphpad Prism and MATLAB. Two-tailed t-test was used in Figure S3C. Ordinary one-way ANOVA, followed by Tukey's multiple comparisons test was used for comparing multiple groups with similar variance as determined by Brown–Forsythe test for Figures 3I–3L, 4S, 4T, 5D, and 5E. Ordinary one-way ANOVA, followed by Games-Howell's multiple comparisons test was used for comparing multiple groups with different variance as determined by Brown–Forsythe test for Figure 5F. Kolmogorov–Smirnov test was used in Figures 6J and 6K. One-sided t-test was used in Figures 6L, 7G, 7H, S7A, S7B, S7D, and S7E. One asterisk denotes a significance of $P>0.05$, two asterisks represent $P>0.01$, and three asterisks are $P>0.001$. Graphs in Figures 1, 2, 3, 4, and 5 were generated using Graphpad Prism. Plots in Figure 6 were generated through Python followed by MATLAB. Plots in Figure 7 were made using MATLAB. Figures were designed in Adobe Illustrator. All confocal images belonging to the same experiment were acquired using the exact same settings. For visualization purposes, brightness adjustments were applied using FIJI to the confocal images shown in the figure panels. All quantitative analyses were carried out on unadjusted raw images. All fly crosses were repeated at least twice, and ovary dissections and staining were repeated at least three times. Sample size was not predetermined by statistical methods, but we used prior knowledge to estimate minimum sample size. The experiments were not randomized. Investigators were not blinded.